Available online at www.sciencedirect.com
ScienceDirect
Journal of the Mechanics and Physics of Solids 56 (2008) 1511–1533
JOURNAL OF THE MECHANICS AND PHYSICS OF SOLIDS
www.elsevier.com/locate/jmps

Multiscale cohesive failure modeling of heterogeneous adhesives

Karel Matouš[a,b,*], Mohan G. Kulkarni[b], Philippe H. Geubelle[b]

[a]*Computational Science and Engineering[1], University of Illinois at Urbana-Champaign, Urbana, IL 61801, USA*
[b]*Department of Aerospace Engineering, University of Illinois at Urbana-Champaign, Urbana, IL 61801, USA*

Received 16 April 2007; received in revised form 3 August 2007; accepted 13 August 2007

Abstract

A novel multiscale cohesive approach that enables prediction of the macroscopic properties of heterogeneous thin layers is presented. The proposed multiscale model relies on the Hill's energy equivalence lemma, implemented in the computational homogenization scheme, to couple the micro- and macro-scales and allows to relate the homogenized cohesive law used to model the failure of the adhesive layer at the macro-scale to the complex damage evolution taking place at the micro-scale. A simple isotropic damage model is used to describe the failure processes at the micro-scale. We establish the upper and lower bounds on the multiscale model and solve several examples to demonstrate the ability of the method to extract physically based macroscopic properties.

Keywords: Multiscale modeling; Hill's lemma; Computational homogenization; Cohesive model; Heterogeneous adhesives

1. Introduction

The addition of heterogeneities in thermoset polymer-based adhesives has received increasing attention in a wide range of engineering applications. In many of these applications, second-phase constituents are added to improve the fracture properties of the usually brittle adhesive layer, often considered as the weak link of the bonded structure. In that line of work, thermosetting polymers have been combined with a variety of reinforcements such as rubber particles (Dean et al., 2004), natural fibers (Ferreira et al., 2005), carbon nanotubes (Meguid and Sun, 2004), glass fibers (Zhao et al., 2000) and nanoparticles (Zhao, 2007). Beyond the improvement of the fracture properties, heterogeneities have been introduced in adhesive systems to achieve multifunctionality. For example, silver flakes (Xu et al., 2003) have been added to improve the thermal and/or electrical conductivity of adhesives in satellite applications. Another, more recent example involves extending the fatigue life of adhesive systems through the incorporation of self-healing capability by embedding micro-capsules filled with a healing agent and a living catalyst in an epoxy-based matrix (White et al., 2001).

*Corresponding author. Computational Science and Engineering, University of Illinois at Urbana-Champaign, Urbana, IL 61801, USA. Tel.: +1 217 333 8448.
E-mail addresses: matous@uiuc.edu (K. Matouš), mkulkar2@uiuc.edu (M.G. Kulkarni), geubelle@uiuc.edu (P.H. Geubelle).
URL: http://www.csar.uiuc.edu/~matous/ (K. Matouš).
[1]NSF, CMS 0527965; U.S. Department of Energy, B523819.

0022-5096/$ - see front matter © 2007 Elsevier Ltd. All rights reserved.
doi:10.1016/j.jmps.2007.08.005

The increasing use of adhesively bonded joints in critical structural applications necessitates the development of reliable and practical integrity assessment tools. Due to the very high length-to-thickness ratio characterizing bonded joints, the cohesive finite element (CFE) method (Camacho and Ortiz, 1996; Needleman, 1990b; Geubelle and Baylor, 1998), which collapses the adhesive layer to a single curve (in 2D analyses) or a surface (in 3D), appears to be a natural choice for the numerical analysis of bonded structures. However, the key component of the CFE model, the cohesive law describing the progressive failure of the adhesive layer, is, in most cases, chosen arbitrarily, in a purely phenomenological or mathematically convenient manner. Examples of common cohesive laws include bilinear (Geubelle and Baylor, 1998), exponential (Needleman, 1990b) and trapezoidal (Ferracin et al., 2003) relations between the cohesive tractions acting along the cohesive interface and the resulting displacement jumps.

However, the complexity of the failure processes taking place in heterogeneous adhesives suggests the need of a different approach in the extraction of the macroscopic cohesive failure model. The heterogeneous micro-structure couples the fracture events across scales and it is important that the cohesive law be representative of these intricate processes. For example, in the case of rubber-modified resins, a clear damage zone is observed as a result of cavitation in rubber particles, while for carbon-nanotube-modified polymers, crack bridging plays an important role. Clearly, a multiscale approach capable of relating the complex micro-scale failure events occurring in the adhesive layer to the macroscopic cohesive law appears as the only viable option.

To model thin layers, such as adhesives or imperfect contacting bodies, several procedures have been proposed: Bouchitte et al. (1991) used the boundary homogenization method to capture the effect of asperities on the contact of elasto-plastic and rigid bodies; Licht and Michaille (1997) and Lebon et al. (1998) adopted an energy minimization principle with asymptotic highly oscillating functions to deduce a constraint condition between bodies when the thickness and stiffness of an adhesive tend to zero. More related to the proposed multiscale approach described in this paper is the asymptotic method adopted by Lebon et al. (2004) to deduce interface laws for the mechanical behavior of thin layers. Their analysis employs asymptotic decomposition of the displacements and the stresses in both adhered and adhesive layer. However, all of the methods mentioned above assume the homogeneous material and thus are not directly applicable to heterogeneous adhesives considered in this work. To our knowledge, the literature only contains a limited number of numerical analyses of damage evolution in thin heterogeneous adhesive layers. Of those, most have focused on a single-scale micro-level investigation of the damage processes (Chew et al., 2004; de Moura et al., 2006; Shi, 2006). However, the computational detail involved in these studies renders them prohibitively expensive and the direct link between the scales is not easily obtained.

The multiscale cohesive framework presented hereafter aims at relating microscopic failure processes taking place in heterogeneous adhesives to the macroscopic cohesive failure model. The macro- and micro-scales are linked using an energy-based computational homogenization approach, which relies on an implementation of Hill's stationarity condition. Our scheme, compared to work presented above, does not place any restrictions on the stiffness of individual constituents. Heterogeneous adhesives with randomly distributed inclusions of an arbitrary shape and size can be investigated. Moreover, a computationally attractive coupling between scales is obtained. Although, the examples investigated in this work focus on the constitutive and failure response of heterogeneous adhesive systems, the multiscale homogenization scheme could be extended to other properties such as electrical and thermal conductivities. A detailed description of the multiscale model constitutes the first part of the paper (Section 2) followed, in Section 3, by a description of the damage model used at the micro-scale and a discussion on implementation issues. In Section 4, we compare the multiscale numerical results to the classical micro-mechanics bounds. The multiscale cohesive framework is then applied in Section 5 to model various heterogeneous adhesive systems involving embedded stiff and soft particles.

2. Multiscale cohesive model

Consider a body represented by an open set $\Omega \subset \mathbb{R}^{\mathfrak{N}}$ consisting of material points $\boldsymbol{X} \in \mathbb{R}^{\mathfrak{N}}$, $\mathfrak{N}$ being the space dimension. Its boundary is denoted by $\partial\Omega$ and is separable into disjoint subsets $\partial\Omega_{\boldsymbol{u}}$ and $\partial\Omega_{\boldsymbol{t}}$, where displacement $\bar{\boldsymbol{u}}$ and tractions $\bar{\boldsymbol{t}}$ are prescribed, respectively, such that $\partial\Omega = \partial\Omega_{\boldsymbol{u}} \cup \partial\Omega_{\boldsymbol{t}}$ and $\partial\Omega_{\boldsymbol{u}} \cap \partial\Omega_{\boldsymbol{t}} = \emptyset$. Given an oriented sub-manifold Γ_{c} of dimension $\mathfrak{N}-1$ (i.e., a surface in three dimensions or a curve in two

dimensions) with a unit normal $\boldsymbol{N}(\boldsymbol{X})$, let l_c be the characteristic (effective) thickness defined by

$$l_c = \Psi/\Gamma_c, \tag{1}$$

where Ψ is the volume (area in 2D) of an adhesive layer, $\Psi = \int_\Psi \mathrm{d}\Psi$. The sub-manifold Γ_c introduced above is a mathematical idealization of a heterogeneous adhesive layer and the thickness l_c is strictly positive, $l_c > 0$. Moreover, we assume the adhesive layer to be locally periodic ($Y_{1,2}$-periodic, in-plane Γ_c-periodic) with the period of micro-structure defined by the representative volume element (RVE) and denoted by Θ, as in Fig. 1. We now partition the body into sub-domains, such that

$$\Omega = \Omega^+ \cup \Omega^- \cup \Psi, \tag{2}$$

where $\Omega^\pm$ denote the two homogeneous sub-bodies (adherends) that occupy the plus and minus sides of the cohesive surface, $\Gamma_c^\pm$, respectively (Fig. 1).

2.1. Governing equations

When the deformable solid is subjected to arbitrary loads and boundary conditions, the deformation, stresses and internal state variables vary from point to point in the adhesive layer due to the micro-structural heterogeneity. We assume that all quantities at the micro-scale in the bond line are dependent on both macro-scale $\boldsymbol{X}$ and micro-scale $\boldsymbol{Y}$ coordinate vectors. We then consider the following hierarchical decomposition of the displacement in the adhesive layer:

$$^A\boldsymbol{u}(\boldsymbol{X},\boldsymbol{Y}) = {}^0\boldsymbol{u}(\boldsymbol{X}) + {}^1\boldsymbol{u}(\boldsymbol{Y}), \tag{3}$$

where $^0\boldsymbol{u}(\boldsymbol{X})$ represents the macroscopic displacement and $^1\boldsymbol{u}(\boldsymbol{Y})$ denotes the microscopic fluctuation displacement. The displacement field in the adhesive layer $^A\boldsymbol{u}$ belongs to the space

$$\begin{aligned}
\mathscr{V}_{\Psi\times\Theta} &= \{{}^A\boldsymbol{u}(\boldsymbol{X},\boldsymbol{Y})|{}^A\boldsymbol{u}(\boldsymbol{X},\boldsymbol{Y}) \in [H^1(\Psi)\times L^2(\Psi;V_\Theta)]^{\mathfrak{N}},\\
&\quad {}^1\boldsymbol{u}(\bullet,\boldsymbol{Y}) \text{ is } Y_{1,2}\text{-periodic}, \ {}^A\boldsymbol{u}(\bullet,\boldsymbol{Y})|_{\Gamma_c^\pm} = {}^0\boldsymbol{u}(\boldsymbol{X})\},\\
\mathscr{V}_\Psi &= \{{}^0\boldsymbol{u}(\boldsymbol{X})|{}^0\boldsymbol{u}(\boldsymbol{X}) \in [H^1(\Psi)]^{\mathfrak{N}}\},\\
\mathscr{V}_\Theta &= \{{}^1\boldsymbol{u}(\boldsymbol{Y})|{}^1\boldsymbol{u}(\boldsymbol{Y}) \in [H^1(\Theta)]^{\mathfrak{N}}, {}^1\boldsymbol{u}(\boldsymbol{Y}) \text{ is } Y_{1,2}\text{-periodic},\\
&\quad {}^1\boldsymbol{u}(\boldsymbol{Y})|_{\Gamma_c^\pm} = \boldsymbol{0}\},
\end{aligned} \tag{4}$$

whereas the displacement in the sub-domains $\Omega^\pm$ lies in the space $\mathscr{V}_\Omega$ defined by

$$\mathscr{V}_\Omega = \{\boldsymbol{u}(\boldsymbol{X})|\boldsymbol{u}(\boldsymbol{X}) \in [H^1(\Omega)]^{\mathfrak{N}}, \boldsymbol{u}(\boldsymbol{X}) = \bar{\boldsymbol{u}} \text{ on } \partial\Omega_{\boldsymbol{u}}\}, \tag{5}$$

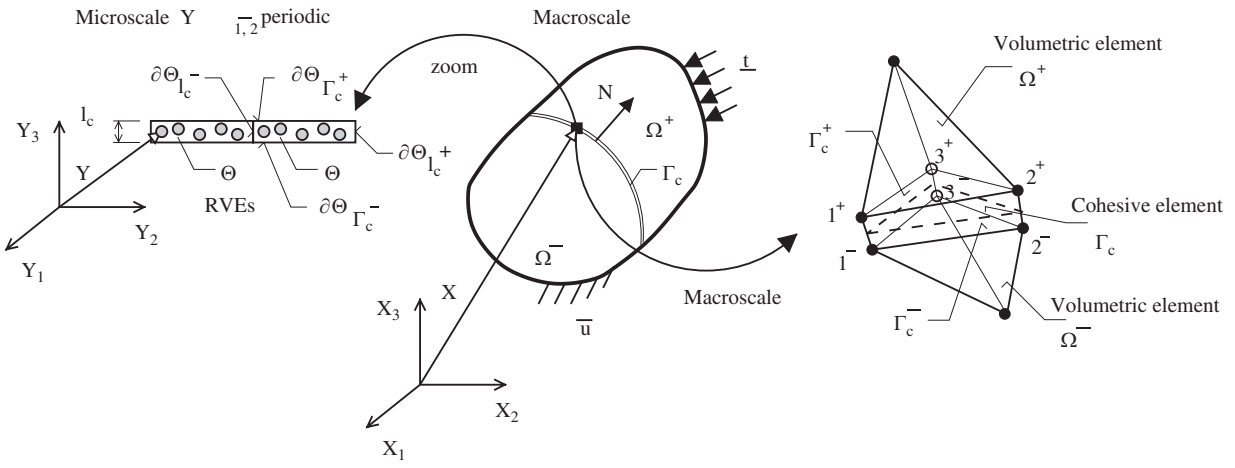

Fig. 1. Microscopic and macroscopic domains with the idealized adhesive band, and geometry of macroscopic cohesive element.

and $H^1(\Omega)$ is the Sobolev space $W^{1,2}(\Omega)$, i.e., $H^1(\Omega)=\{\boldsymbol{u}\in L^2(\Omega)\colon \forall|\boldsymbol{\alpha}|\leqslant 1, \partial_{\boldsymbol{x}}^{\boldsymbol{\alpha}}\boldsymbol{u}\in L^2(\Omega)\}$ where, $\boldsymbol{\alpha}$, $|\boldsymbol{\alpha}|$, and the derivatives $\partial_{\boldsymbol{x}}^{\boldsymbol{\alpha}}$ are taken in a weak sense. Likewise, $H^1(\Psi)=\{{}^0\boldsymbol{u}\in L^2(\Psi)\colon \forall|\boldsymbol{\alpha}|\leqslant 1, \partial_{\boldsymbol{x}}^{\boldsymbol{\alpha}}{}^0\boldsymbol{u}\in L^2(\Psi)\}$ and $H^1(\Theta)=\{{}^1\boldsymbol{u}\in L^2(\Theta)\colon \forall|\boldsymbol{\alpha}|\leqslant 1, \partial_{\boldsymbol{x}}^{\boldsymbol{\alpha}}{}^1\boldsymbol{u}\in L^2(\Theta)\}$. Similar space decomposition has been proposed by Hughes (1995) in his work on the multiscale variational principle. Further information on the space selection can be found in Bensoussan et al. (1978) and Hughes (1995).

The corresponding boundary value problem is described by the following set of governing equations:

$$
\left.\begin{aligned}
&\operatorname{div}(\boldsymbol{\sigma})+\boldsymbol{f}=\boldsymbol{0} && \text{in } \Omega^{\pm}\\
&\boldsymbol{\sigma}=\boldsymbol{L}\colon\boldsymbol{\varepsilon} && \text{in } \Omega^{\pm}\\
&\boldsymbol{\varepsilon}=\nabla_X^{\mathrm{s}}\boldsymbol{u} && \text{in } \Omega^{\pm}
\end{aligned}\right\}\ \text{adherends},
$$

$$
\left.\begin{aligned}
&\operatorname{div}(\boldsymbol{\tau})=\boldsymbol{0} && \text{in } \Psi\\
&\boldsymbol{\tau}=\mathbb{L}\colon[{}^0\boldsymbol{\varepsilon}+{}^1\boldsymbol{\varepsilon}] && \text{in } \Psi\\
&{}^0\boldsymbol{\varepsilon}=\nabla_X^{\mathrm{s}}{}^0\boldsymbol{u} && \text{in } \Psi\\
&{}^1\boldsymbol{\varepsilon}=\nabla_Y^{\mathrm{s}}{}^1\boldsymbol{u} && \text{in } \Psi
\end{aligned}\right\}\ \text{adhesive},
$$

$$
\left.\begin{aligned}
&\boldsymbol{N}\cdot\boldsymbol{\sigma}|_{\Gamma_{\mathrm{c}}^{\pm}}+\boldsymbol{N}\cdot\boldsymbol{\tau}|_{\Gamma_{\mathrm{c}}^{\pm}}=\boldsymbol{0} && \text{on } \Gamma_{\mathrm{c}}^{\pm}\\
&\boldsymbol{\sigma}\cdot\boldsymbol{n}=\bar{\boldsymbol{t}} && \text{on } \partial\Omega_t\\
&\boldsymbol{u}=\bar{\boldsymbol{u}} && \text{on } \partial\Omega_u
\end{aligned}\right\}\ \text{boundary conditions},
\tag{6}
$$

where $\operatorname{div}(\bullet)$ is the divergence operator, $\boldsymbol{\sigma}$ and $\boldsymbol{\varepsilon}$ are the stress and strain tensors in $\Omega^{\pm}$ and $\boldsymbol{\tau}$ denotes the stress tensor in the adhesive layer Ψ. The symbols ∇_X^{s} and ∇_Y^{s} represent the symmetric gradient operators with respect to $\boldsymbol{X}$ and $\boldsymbol{Y}$ coordinates, respectively. $\boldsymbol{L}(\boldsymbol{X})$ denotes the symmetric material tensor for the homogeneous adherends and $\mathbb{L}(\boldsymbol{X},\boldsymbol{Y})$ is the spatially dependent instantaneous secant stiffness tensor of the interface. $\boldsymbol{f}(\boldsymbol{X})$ denotes the body force vector and $\bar{\boldsymbol{t}}(\boldsymbol{X})$ represents the prescribed macroscopic traction vector on the boundary $\partial\Omega_{\mathrm{t}}$. We also consider the Dirichlet boundary conditions $\bar{\boldsymbol{u}}$ on $\partial\Omega_u$.

2.2. Space dimension reduction

In order to approximate the macroscopic strain tensor ${}^0\boldsymbol{\varepsilon}$ in the adhesive layer, we introduce the linear cohesive layer kinematics. Strains are then derived as layer thickness averages, from the relative displacements of the top and bottom sub-domains, as shown in Fig. 2. Thus, the average strains in the adhesive layer become:

$$
{}^0\varepsilon_{11}=\nabla_{X_1}^{\mathrm{s}}{}^0u_1\approx\tfrac{1}{2}(\nabla_{X_1}^{\mathrm{s}}{}^0u_1^{+}+\nabla_{X_1}^{\mathrm{s}}{}^0u_1^{-}),
$$

$$
{}^0\varepsilon_{22}=\nabla_{X_2}^{\mathrm{s}}{}^0u_2\approx\tfrac{1}{2}(\nabla_{X_2}^{\mathrm{s}}{}^0u_2^{+}+\nabla_{X_2}^{\mathrm{s}}{}^0u_2^{-}),
$$

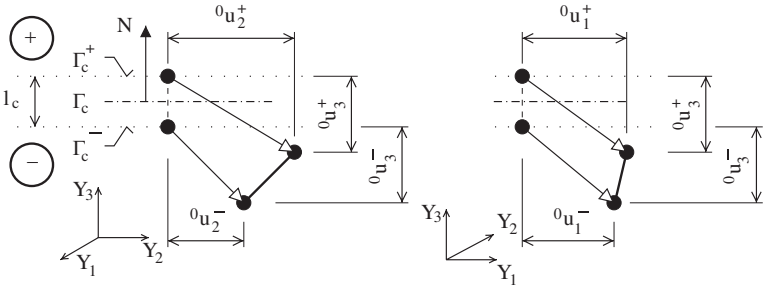

Fig. 2. Adhesive layer kinematics.

$$
\begin{aligned}
{}^0\varepsilon_{12} &= {}^0\varepsilon_{21} = \tfrac{1}{2}(\nabla^{\mathrm{s}}_{X_2}{}^0u_1 + \nabla^{\mathrm{s}}_{X_1}{}^0u_2)\\
&\approx \tfrac{1}{2}(\tfrac{1}{2}(\nabla^{\mathrm{s}}_{X_2}{}^0u_1^+ + \nabla^{\mathrm{s}}_{X_2}{}^0u_1^-) + \tfrac{1}{2}(\nabla^{\mathrm{s}}_{X_1}{}^0u_2^+ + \nabla^{\mathrm{s}}_{X_1}{}^0u_2^-)),
\end{aligned}
$$

$$
\begin{aligned}
{}^0\varepsilon_{33} &\approx \frac{1}{l_{\mathrm{c}}}({}^0u_3^+ - {}^0u_3^-) = \frac{1}{l_{\mathrm{c}}}\lfloor {}^0u_3\rceil,\\
{}^0\varepsilon_{13} = {}^0\varepsilon_{31} &\approx \frac{1}{2}\frac{1}{l_{\mathrm{c}}}({}^0u_1^+ - {}^0u_1^-) = \frac{1}{2}\frac{1}{l_{\mathrm{c}}}\lfloor {}^0u_1\rceil,\\
{}^0\varepsilon_{23} = {}^0\varepsilon_{32} &\approx \frac{1}{2}\frac{1}{l_{\mathrm{c}}}({}^0u_2^+ - {}^0u_2^-) = \frac{1}{2}\frac{1}{l_{\mathrm{c}}}\lfloor {}^0u_2\rceil,
\end{aligned}
\tag{7}
$$

where $\lfloor\bullet\rceil = (\bullet^+ - \bullet^-)$ denotes the jump operator. Based on such a kinematics, let us introduce the following notation for the adhesive layer strain tensor:

$$
{}^0\boldsymbol{\varepsilon} \equiv \frac{1}{l_{\mathrm{c}}}\lfloor\lfloor {}^0\boldsymbol{u}\rceil\rceil = \frac{1}{l_{\mathrm{c}}}\begin{bmatrix} l_{\mathrm{c}}{}^0\varepsilon_{11} & l_{\mathrm{c}}{}^0\varepsilon_{12} & \frac{1}{2}\lfloor {}^0u_1\rceil \\ l_{\mathrm{c}}{}^0\varepsilon_{21} & l_{\mathrm{c}}{}^0\varepsilon_{22} & \frac{1}{2}\lfloor {}^0u_2\rceil \\ \frac{1}{2}\lfloor {}^0u_1\rceil & \frac{1}{2}\lfloor {}^0u_2\rceil & \lfloor {}^0u_3\rceil \end{bmatrix}. \tag{8}
$$

As apparent from Eq. (7), $({}^0\varepsilon_{11}, {}^0\varepsilon_{22}, {}^0\varepsilon_{12})$ and $({}^0\varepsilon_{33}, {}^0\varepsilon_{13}, {}^0\varepsilon_{32})$ can be referred as in-plane and out-of-plane components, respectively. For an adhesive layer, the out-of-plane strains are usually dominant and the in-plane components are often neglected (Matouš and Dvorak, 2002a, b). Remember the relationship between engineering and tensorial shear strains $\gamma_{ij} = 2\varepsilon_{ij}$, $\forall i \neq j$.

After applying standard variational methods to the problem described by Eq. (6), the principle of virtual work reads

$$
\underbrace{\int_{\Omega^\pm} \boldsymbol{\sigma}\colon \nabla^{\mathrm{s}}_X \delta\boldsymbol{u}\,\mathrm{d}\Omega}_{\text{adherend}} + \underbrace{\int_{\Psi} \boldsymbol{\tau}\colon \nabla^{\mathrm{s}}_X \delta\boldsymbol{u}\,\mathrm{d}\Psi}_{\text{adhesive}} - \int_{\Omega^\pm} \boldsymbol{f}\cdot\delta\boldsymbol{u}\,\mathrm{d}\Omega - \int_{\partial\Omega_t} \bar{\boldsymbol{t}}\cdot\delta\boldsymbol{u}\,\mathrm{d}A = 0 \tag{9}
$$

for all admissible variations $\delta\boldsymbol{u}$ satisfying

$$
\mathscr{V} = \{\delta\boldsymbol{u} | \delta\boldsymbol{u} \in [H^1(\Omega)]^{\mathfrak{N}}, \delta\boldsymbol{u} = \boldsymbol{0} \text{ on } \partial\Omega_{\boldsymbol{u}}\}. \tag{10}
$$

In the multiscale variational principle (Hughes, 1995), the space decomposition is also performed for weighting functions and an additional Euler–Lagrange equation is obtained for fine scale unknowns. Here, we decompose only the displacement space and multiscale coupling is accomplished differently, as described later. We now focus our attention on the second term in Eq. (9). Integrating by parts, applying the divergence theorem and approximating the volume integral over Ψ by $\int_\Psi \bullet\,\mathrm{d}\Psi \approx l_{\mathrm{c}}\int_{\Gamma_{\mathrm{c}}} \bullet\,\mathrm{d}A$, we obtain

$$
\int_{\Psi} \boldsymbol{\tau}\colon \nabla^{\mathrm{s}}_X \delta\boldsymbol{u}\,\mathrm{d}\Psi = -\underbrace{l_{\mathrm{c}}\int_{\Gamma_{\mathrm{c}}} \nabla^{\mathrm{s}}_X\cdot\boldsymbol{\tau}\cdot\delta\boldsymbol{u}\,\mathrm{d}A}_{\approx 0} + \int_{\partial\Psi} \boldsymbol{N}\cdot\boldsymbol{\tau}\cdot\delta\boldsymbol{u}\,\mathrm{d}A. \tag{11}
$$

Note that first term can be neglected since the cohesive layer thickness is assumed to be much smaller than the other body dimensions. Assuming that no external forces are acting on the outside boundary, $\partial\Theta_{l_{\mathrm{c}}^\pm}$, of the adhesive bond line with thickness l_{c}, the remaining term can be rewritten as

$$
\int_{\partial\Psi} \boldsymbol{N}\cdot\boldsymbol{\tau}\cdot\delta^0\boldsymbol{u}\,\mathrm{d}A = \int_{\Gamma_{\mathrm{c}}} \boldsymbol{t}\cdot\lfloor\delta^0\boldsymbol{u}\rceil\,\mathrm{d}A, \tag{12}
$$

which implies that $\boldsymbol{N}\cdot\boldsymbol{\tau}|_{\Gamma_{\mathrm{c}}^+} + \boldsymbol{N}\cdot\boldsymbol{\tau}|_{\Gamma_{\mathrm{c}}^-} = \boldsymbol{0}$ as $l_{\mathrm{c}} \to 0$. Thus, we arrive at the classical cohesive contribution and the principle of virtual work at the macro-scale yields

$$
\underbrace{\int_{\Omega^\pm} \boldsymbol{\sigma}\colon \nabla^{\mathrm{s}}_X \delta^0 u\,\mathrm{d}\Omega}_{\text{volumetric contribution}} + \underbrace{\int_{\Gamma_{\mathrm{c}}} \boldsymbol{t}\cdot\lfloor\delta^0\boldsymbol{u}\rceil\,\mathrm{d}A}_{\text{cohesive contribution}} - \int_{\Omega^\pm} \boldsymbol{f}\cdot\delta^0\boldsymbol{u}\,\mathrm{d}\Omega - \int_{\partial\Omega_t} \bar{\boldsymbol{t}}\cdot\delta^0\boldsymbol{u}\,\mathrm{d}A = 0 \tag{13}
$$

for all admissible variations $\delta^0\boldsymbol{u}$ satisfying Eq. (10). Here, we take advantage of the arbitrariness of the weighting functions and set $\delta\boldsymbol{u} = \delta^0\boldsymbol{u}(\boldsymbol{X})$. The cohesive contribution term, in the principal of virtual work (Eq. (13)), can also be deduced from the unbounded part of the gradient of the weighting function (Wells and Sluys, 2001). Note, however, that in this work, the discontinuity is always contained between volumetric elements as opposed to the generalized finite element method (Wells and Sluys, 2001). Hence, the test functions, $\delta^0\boldsymbol{u}$, belong to the space of bounded variations since they are discontinuous across the interface. Note that the cohesive tractions $\boldsymbol{t}$ perform work on the displacement jumps or "opening displacements" over the cohesive surface. The macroscopic cohesive element is shown schematically in Fig. 1.

2.3. Link between macro- and micro-scale

In this subsection, a theoretical framework is presented for relating the deformation at the micro-scale to that at the macro-scale. We use the standard argument of scale separation, since the macroscopic problem is defined on a scale with characteristic length $l_{\text{macro}} \approx \mathcal{O}(\Gamma_c)$ (scale of adherends) while the micro-structure is of size $l_{\text{micro}} \approx \mathcal{O}(l_c)$ (thickness of adhesive) as depicted in Fig. 1. The scale separation requires that $l_{\text{micro}}/l_{\text{macro}} \ll 1$. Thus, the micro-to-macro transitions can be described by the notion of a homogenized macro-continuum with locally attached heterogeneous micro-structure (RVE). In this work, computational homogenization is used to link the micro-scale to the macro-scale.

The behavior of a material point at the macro-scale can be linked to the micro-scale through the following energy condition. The potential energy on the micro- and macro-scales is minimized when the following condition of stationarity (Hill's lemma) is met:

$$\inf_{\lfloor {}^0\boldsymbol{u}\rceil} \underline{\psi}(\lfloor {}^0\boldsymbol{u}\rceil) = \inf_{{}^0\boldsymbol{\varepsilon}} \inf_{{}^1\boldsymbol{u}} \frac{1}{|\Theta|}\int_\Theta \psi({}^0\boldsymbol{\varepsilon}(\lfloor {}^0\boldsymbol{u}\rceil) + \nabla_Y^s\, {}^1\boldsymbol{u})\,\mathrm{d}\Theta \tag{14}$$

and

$$\begin{aligned} &{}^0\boldsymbol{\varepsilon}(\lfloor {}^0\boldsymbol{u}\rceil) \in \mathfrak{L}^+, \\ &{}^1\boldsymbol{u} \in \mathscr{V}_\Theta, \end{aligned} \tag{15}$$

where ψ and $\underline{\psi}$ represent the free energy density on the micro- and macro-scales, respectively, and $\mathfrak{L}^+$ is the space of second order tensors with positive determinant. By recourse to Coleman and Noll's method (Lubliner, 1972, 1973), it is possible to show that the constitutive laws relating the stress to the free energy density on the micro-scale, and the tractions to the homogenized free energy density $\underline{\psi}$ on the macro-scale are

$$\boldsymbol{\tau} = \frac{\partial\psi}{\partial^A\boldsymbol{\varepsilon}} \quad \text{and} \quad \boldsymbol{t} = \frac{\partial\,\underline{\psi}}{\partial\lfloor {}^0\boldsymbol{u}\rceil}, \tag{16}$$

where ${}^A\boldsymbol{\varepsilon} = ({}^0\boldsymbol{\varepsilon} + {}^1\boldsymbol{\varepsilon})$ denotes strain in the adhesive layer. Applying standard variational principles to Eq. (14) and keeping in mind that the variations of the macro-scale displacement jump $\lfloor\delta^0\boldsymbol{u}\rceil$, $\delta^0\boldsymbol{\varepsilon}(\lfloor\delta^0\boldsymbol{u}\rceil)$ and the micro-scale fluctuation displacements $\delta^1\boldsymbol{u}$ are independent, we arrive at the variational energy condition (see, for example, references Hill, 1985; Miehe et al., 2002),

$$\begin{aligned} \mathscr{R}_{\lfloor {}^0\boldsymbol{u}\rceil} &= \left[\boldsymbol{N}\cdot\left(\frac{1}{|\Theta|}\int_\Theta \boldsymbol{\tau}\,\mathrm{d}\Theta\right) - \boldsymbol{t}\right]\cdot\lfloor\delta^0\boldsymbol{u}\rceil = 0, \\ \mathscr{R}_{{}^1\boldsymbol{u}} &= \frac{1}{|\Theta|}\int_\Theta \boldsymbol{\tau}\colon\nabla_Y^s\delta^1\boldsymbol{u}\,\mathrm{d}\Theta = 0 \end{aligned} \tag{17}$$

and

$$\delta^1\boldsymbol{u} \in [H^1(\Theta)]^{\mathfrak{N}}, \quad \delta^1\boldsymbol{u}|_{\partial\Theta_{\Gamma_c^\pm}} = \boldsymbol{0}, \quad \delta^1\boldsymbol{u} = \text{periodic} \quad \text{on } \partial\Theta_{l_c^\pm}, \tag{18}$$

where $\partial\Theta = \partial\Theta_{\Gamma_c^+} \cup \partial\Theta_{l_c^+} \cup \partial\Theta_{\Gamma_c^-} \cup \partial\Theta_{l_c^-}$ being the boundary of Θ (Fig. 1). Here, we take an advantage of the arbitrariness of the displacement jump variation and use

$$\delta^0\boldsymbol{\varepsilon}(\lfloor\delta^0\boldsymbol{u}\rceil) = \frac{1}{l_c}\boldsymbol{N}\otimes\lfloor\delta^0\boldsymbol{u}\rceil, \tag{19}$$

where $\otimes$ represents the dyadic vector product. In other words, the volume average of the variation of the work performed on the RVE equals the local variation of the work on the macro-scale, and the micro-scale

fluctuation field does not contribute to the average variation in the work. Furthermore, due to the arbitrariness of $\lfloor \delta^0 \boldsymbol{u} \rceil$, Eq. (17a) indicates that the macroscopic tractions are equal to the volume average of the stress at the micro-scale contracted with the normal. It should also be noted that Eq. (17b) is the weak form of the equilibrium equation on the micro-scale for purely kinematic boundary conditions (as in this work). Eqs. (17) are in general nonlinear, based on the mechanical behavior of the individual constituents. Possible inelastic mechanical processes, characterized by the secant stiffness tensor $\mathbb{L}(\boldsymbol{X}, \boldsymbol{Y})$, include plasticity, nonlinear viscoelasticity and/or damage. Mechanical response of a heterogeneous adhesive layer discussed in this paper is described in Section 3.1.

In general, the Helmholtz free energy per unit volume stored in the system depends on the elastic behavior, inelastic state of deformation, and temperature. For the sake of simplicity, we neglect thermal effects and adopt the usual assumption that the elastic potential is unaffected by the inelastic processes. In addition, it is assumed that the elastic behavior is linear and elastic strains are small, typical for epoxy adhesives.

Based on such an observation, one can define the potential, referred to in Eqs. (14) and (16), as

$$\psi({}^A\boldsymbol{\varepsilon}) = \tfrac{1}{2}({}^0\boldsymbol{\varepsilon} + {}^1\boldsymbol{\varepsilon}) : \mathbb{L} : ({}^0\boldsymbol{\varepsilon} + {}^1\boldsymbol{\varepsilon}), \tag{20}$$

and, according to Eq. (16), the micro-scale constitutive stress strain relation used in Eq. (6) reads

$$\boldsymbol{\tau} = \frac{\partial \psi}{\partial {}^A\boldsymbol{\varepsilon}} = \mathbb{L} : [{}^0\boldsymbol{\varepsilon} + {}^1\boldsymbol{\varepsilon}]. \tag{21}$$

Assuming that variational equations (17) are satisfied, the macroscopic traction vector is then given by

$$\boldsymbol{t} = \boldsymbol{N} \cdot \left\{ \frac{1}{|\Theta|} \int_\Theta \mathbb{L} : \left[\frac{1}{l_c} \lfloor \lfloor {}^0\boldsymbol{u} \rceil \rceil + \nabla^s_Y {}^1\boldsymbol{u} \right] \mathrm{d}\Theta \right\}, \tag{22}$$

where $\boldsymbol{t}^T = \{t_{t_1}, t_{t_2}, t_n\}$. As one can see, the macroscopic cohesive vector depends on both macro- and micro-scale contributions. For the homogeneous adhesive layer, where $\mathbb{L}(\boldsymbol{X}, \boldsymbol{Y}) = \mathbb{L}(\boldsymbol{X})$ we get

$$\boldsymbol{t} = \frac{1}{l_c} \boldsymbol{N} \cdot \{ \mathbb{L} : \lfloor \lfloor {}^0\boldsymbol{u} \rceil \rceil \}, \tag{23}$$

and the following constraint on the fluctuation field results

$$\frac{1}{|\Theta|} \int_\Theta \nabla^s_Y {}^1\boldsymbol{u} \, \mathrm{d}\Theta = \boldsymbol{0} \;\Rightarrow\; \frac{1}{|\Theta|} \int_{\partial\Theta} \frac{1}{2} [\boldsymbol{N}_\Theta \otimes {}^1\boldsymbol{u} + {}^1\boldsymbol{u} \otimes \boldsymbol{N}_\Theta] \, \mathrm{d}A = \boldsymbol{0}, \tag{24}$$

where $\boldsymbol{N}_\Theta$ is the outward normal of the micro-system at $\boldsymbol{Y} \in \partial\Theta$. Note that along the top and bottom edges of the layer, i.e., $\forall\ \boldsymbol{Y} \in \partial\Theta_{\Gamma_c^\pm}$, $\boldsymbol{N}_\Theta \equiv \boldsymbol{N}$ (Fig. 2). Non-trivial boundary conditions for the fluctuation displacement defined by Eq. (4) satisfy the constraint (24).

2.4. Linearized form of the macroscopic traction-separation law

An incrementally linearized form of the macroscopic traction-separation law can be defined by linearizing the nonlinear equations (17), where the micro-scale constitutive law (21) is used to relate the strain tensor at the micro-scale, ${}^0\boldsymbol{\varepsilon} + {}^1\boldsymbol{\varepsilon}$, to the stress tensor $\boldsymbol{\tau}$. Linearization of Eq. (17) yields

$$\begin{bmatrix} \mathscr{K}_{11} & \mathscr{K}_{12} \\ \mathscr{K}_{21} & \mathscr{K}_{22} \end{bmatrix}^k \begin{Bmatrix} \lfloor \Delta^0 \boldsymbol{u} \rceil \\ \Delta^1 \boldsymbol{u} \end{Bmatrix} = \begin{Bmatrix} \boldsymbol{t} \\ \boldsymbol{0} \end{Bmatrix}^{k+1} - \begin{Bmatrix} \boldsymbol{t} \\ \mathscr{R}_2 \end{Bmatrix}^k, \tag{25}$$

where

$$\lfloor \delta^0 \boldsymbol{u} \rceil \cdot \mathscr{K}_{11} \equiv \frac{\partial \mathscr{R}_{\lfloor {}^0\boldsymbol{u} \rceil}}{\partial \lfloor {}^0\boldsymbol{u} \rceil}, \quad \lfloor \delta^0 \boldsymbol{u} \rceil \cdot \mathscr{K}_{12} \equiv \frac{\partial \mathscr{R}_{\lfloor {}^0\boldsymbol{u} \rceil}}{\partial {}^1\boldsymbol{u}},$$

$$\delta^1 \boldsymbol{u} \cdot \mathscr{K}_{21} \equiv \frac{\partial \mathscr{R}_{{}^1\boldsymbol{u}}}{\partial \lfloor {}^0\boldsymbol{u} \rceil}, \quad \delta^1 \boldsymbol{u} \cdot \mathscr{K}_{22} \equiv \frac{\partial \mathscr{R}_{{}^1\boldsymbol{u}}}{\partial {}^1\boldsymbol{u}}, \quad \delta^1 \boldsymbol{u} \cdot \mathscr{R}_2 \equiv \mathscr{R}_{{}^1\boldsymbol{u}},$$

and, for the $(k+1)$th iteration, the macroscopic displacement jump, the micro-continuum fluctuation displacement field, and the macroscopic traction vector are updated as $\lfloor {}^0\boldsymbol{u}\rceil^{k+1} = \lfloor {}^0\boldsymbol{u}\rceil^k + \lfloor \Delta^0\boldsymbol{u}\rceil$, ${}^1\boldsymbol{u}^{k+1} = {}^1\boldsymbol{u}^k + \Delta^1\boldsymbol{u}$, and $\boldsymbol{t}^{k+1} = \boldsymbol{t}^k + \Delta\boldsymbol{t}$, respectively. Eliminating the fluctuation displacements $\Delta^1\boldsymbol{u}$ from Eq. (25) provides the incrementally linear macroscopic traction-separation law

$$\Delta\boldsymbol{t} = \mathscr{L}\colon \lfloor \Delta^0\boldsymbol{u}\rceil - (\mathscr{K}_{12}\mathscr{K}_{22}^{-1})^k\colon \mathscr{R}_2^k, \tag{26}$$

where the tangent instantaneous cohesive moduli is

$$\mathscr{L} = (\mathscr{K}_{11} - \mathscr{K}_{12}\mathscr{K}_{22}^{-1}\mathscr{K}_{21})^k. \tag{27}$$

The above linearized form of the macroscopic traction-separation response is useful for computational purposes.

3. Damage model and implementation issues

To illustrate the multiscale cohesive model described in Section 2, we investigate in Section 5 the failure response of model heterogeneous adhesives characterized by a simple isotropic damage law. In this section, we develop the damage evolution model used at the micro-scale and outline the numerical implementation of multiscale cohesive approach.

3.1. Irreversible isotropic damage law

The damage model employs irreversible thermodynamics and the internal state variables theory. Similar formulations have been applied to a variety of continuum damage mechanics problems (Lemaitre, 1985; Simo and Ju, 1987a, b); Ju, 1989; Lubarda and Krajcinovic, 1995; Matouš, 2003). To introduce damage behavior, let us consider the free energy potential given by Eq. (20) as

$$\psi({}^A\boldsymbol{\varepsilon}, \omega) = (1-\omega)\psi_0({}^A\boldsymbol{\varepsilon}), \tag{28}$$

with

$$\psi_0({}^A\boldsymbol{\varepsilon}) = \tfrac{1}{2}{}^A\boldsymbol{\varepsilon}\colon {}^A\boldsymbol{L}\colon {}^A\boldsymbol{\varepsilon}, \tag{29}$$

where $\psi_0({}^A\boldsymbol{\varepsilon})$ represents the total potential energy function of an undamaged (virgin) material, ω denotes the isotropic damage parameter and ${}^A\boldsymbol{L}(\boldsymbol{X}, \boldsymbol{Y})$ is the elastic stiffness of micro-constituents. Considering only the mechanical loading, the Clausius–Duhem inequality reads

$$-\dot{\psi} + \boldsymbol{\tau}\colon {}^A\dot{\boldsymbol{\varepsilon}} \geqslant 0, \tag{30}$$

and the dissipative inequality is given by (differentiate Eq. (28) and use Eq. (30))

$$\mathfrak{D} = -\dot{\omega}\, Y \geqslant 0, \tag{31}$$

where $Y = -\psi_0({}^A\boldsymbol{\varepsilon})$ denotes the thermodynamic force (damage energy release rate) conjugate to the damage variable $\dot{\omega}$.

To define the onset or continuation of damage, we adopt the approach based on a damage surface analogous to the yield surface used in the theory of plasticity (Bittnar and Šejnoha, 1996; Ju, 1989; Matouš, 2003). The state of damage in the material is governed by the following criterion:

$$g(\bar{Y}, \chi^{\mathrm{t}}) = G(\bar{Y}) - \chi^{\mathrm{t}} \leqslant 0, \quad \bar{Y} = -Y, \ \ \mathrm{t} \in \mathbb{R}^+, \tag{32}$$

where χ^{t} denotes the softening parameter (internal state variable) usually set as $\chi^{\mathrm{t}=0} = 0$. The notation $\bar{Y} = -Y$ is used here for convenience. The function $G(\bar{Y})$, which characterizes the damage process in the material, can possess various mathematical forms and we here adopt a three-parameter Weibull distribution that reads

$$G(\bar{Y}) = 1 - \exp\left[-\left(\frac{\bar{Y} - Y_{\mathrm{in}}}{p_1 Y_{\mathrm{in}}}\right)^{p_2}\right], \tag{33}$$

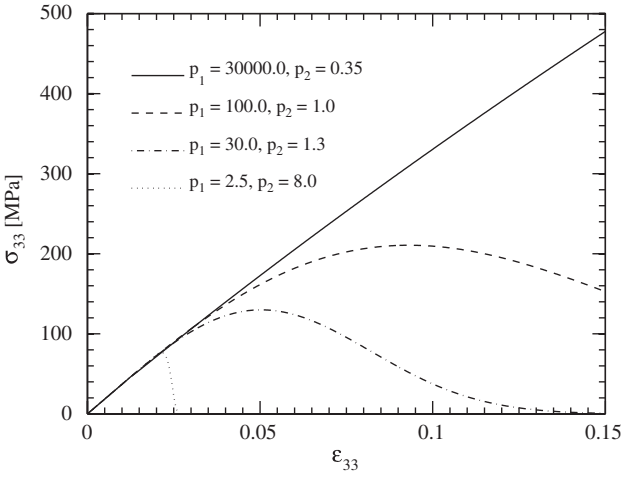

Fig. 3. Illustrative constitutive behaviors obtained by using the Weibull distribution damage function within the isotropic damage model. Other material properties used are $E = 2.4\,\mathrm{GPa}$, $\nu = 0.34$, $Y_{\mathrm{in}} = 0.32\,\mathrm{J/m^3}$ and $\mu = 19.0\,\mathrm{s^{-1}}$.

where Y_{in} denotes the initial threshold (energy barrier), and p_1 and p_2 are non-dimensional scale and shape parameters, respectively. The three-parameter form of above expression enables it to capture a wide range of material behaviors. A few representative constitutive response curves obtained by using the Weibull distribution within the isotropic damage model discussed above are shown in Fig. 3. Note that the exponential form of the damage function (33) makes it infinitely continuously differentiable.

The damage process is derived in terms of the following irreversible, dissipative equation of evolution:

$$\dot{\omega} = \dot{\kappa}\frac{\partial g}{\partial \bar{Y}} = \dot{\kappa}H, \quad H = \frac{\partial G(\bar{Y})}{\partial \bar{Y}}, \tag{34}$$

where $\dot{\kappa}$ is a damage consistency parameter, which defines damage loading/unloading according to the Kuhn–Tucker complementarity conditions:

$$\dot{\kappa} \geqslant 0, \quad g(\bar{Y}, \chi^{\mathrm{t}}) \leqslant 0, \quad \dot{\kappa} g(\bar{Y}, \chi^{\mathrm{t}}) \equiv 0. \tag{35}$$

In addition, we define $\dot{\chi}^{\mathrm{t}} = \dot{\kappa}H$ and the parameter $\dot{\kappa}$ is determined from the consistency condition $\dot{g} = 0$, from which follows

$$\dot{\kappa} = -\dot{Y} \tag{36}$$

and

$$\dot{Y} = -\bar{\boldsymbol{\tau}} : {}^{A}\dot{\boldsymbol{\varepsilon}}, \quad \bar{\boldsymbol{\tau}} \equiv \frac{\boldsymbol{\tau}}{1-\omega}, \tag{37}$$

where $\bar{\boldsymbol{\tau}}$ represents the effective stress tensor. The evolution of the monotonically increasing internal state variable, χ^{t}, is given by

$$\chi^{\mathrm{t}} = \max\left\{\chi^{0}, \max_{s\in(-\infty,\mathrm{t}]} \chi^{s}\right\}, \tag{38}$$

and we assume unloading towards the origin.

It is prevalent that there are well-posedness and uniqueness problems associated with the loss of strong material ellipticity. As a result, the numerical computations exhibit mesh bias, i.e., the solution is sensitive to discretization. The numerical deficiencies may be bypassed by means of the nonlocal model proposed by Pijaudier-Cabot and Bažant (1987) or by viscous regularization (Simo and Ju, 1987a, b; Ju, 1989). In this work, we adopt the approach proposed by Simo and Ju (1987b) based on a viscous damage model.

In particular, the evolution equations for $\dot{\omega}$ and $\dot{\chi}^{\mathrm{t}}$ that govern the visco-damage behavior are obtained by replacing the damage consistency parameter $\dot{\kappa}$ as follows:

$$\dot{\omega} = \dot{\kappa} H \rightarrow \dot{\omega} = \mu\langle\phi(g)\rangle \quad \text{and} \quad \dot{\chi}^{\mathrm{t}} = \dot{\kappa} H \rightarrow \dot{\chi}^{\mathrm{t}} = \mu\langle\phi(g)\rangle, \tag{39}$$

where μ denotes the damage viscosity coefficient. $\phi(g)$ represents the viscous damage flow function with g defined in Eq. (32), and the symbol $\langle\bullet\rangle$ denotes McAuley brackets. As in Ju (1989), we assume a linear viscous damage mechanism, $\phi(g) \equiv g$. As μ goes to zero, we obtain the instantaneous elastic behavior, whereas, for μ approaching infinity, we recover the rate-independent model.

3.2. Numerical implementation

The multiscale cohesive framework developed in Section 2 and the damage model described in Section 3.1 are implemented into conventional finite element framework. Here, we do not numerically solve the macroscopic boundary value problem, Eq. (13). The deformation path of a macroscopic cohesive point is rather predefined by applying a displacement jump, $\lfloor {}^0\boldsymbol{u} \rceil$, across the cohesive interface, and hence, the first Euler–Lagrange equation (17a) is trivially satisfied. Thus, we need to solve only the second equation, Eq. (17b), and the macroscopic tractions can be directly computed using Eq. (22). The numerical implementation involves three issues: the numerical integration of the rate form of the constitutive equations, the consistent linearization of the finite element form of the micro-scale equilibrium equation, and the adaptive load-stepping scheme. These three issues are discussed next.

A key aspect of the numerical scheme is the precision of the incremental update procedure used to integrate the evolution equations (39). The associated computational algorithm follows that of Ju (1989) and is summarized for completeness in Appendix A. Let $\boldsymbol{R}$, $\boldsymbol{B}$, and ${}^1\boldsymbol{U}$ represent the residual, strain-displacement (gradient) matrix, and micro-scale degree-of-freedom vector, respectively. The weak form of the equilibrium equation at the micro-scale (17b) can be discretized to obtain the standard finite element form as

$$\boldsymbol{R}({}^1\boldsymbol{U}) = \frac{1}{|\Theta|}\mathop{\mathbb{A}}_{e=1}^{N_{\mathrm{el}}}\left\{\left[\int_{\Theta^e}\boldsymbol{B}^{\mathrm{T}}\mathbb{L}\boldsymbol{B}\,\mathrm{d}\Theta^e\,{}^1\boldsymbol{U} + \int_{\Theta^e}\boldsymbol{B}^{\mathrm{T}}\mathbb{L}\,\mathrm{d}\Theta^e\,{}^0\boldsymbol{\varepsilon}\right]\right\} = \boldsymbol{0}, \tag{40}$$

where we have made use of Eq. (21) and the secant stiffness tensor is given by $\mathbb{L} = (1-\omega)^A\boldsymbol{L}$. The symbol $\mathbb{A}$ in Eq. (40) represents assembly operator, while N_{el} is the number of finite elements. The second term of the equation represents the contribution from the macro-scale and acts as a forcing term. The nonlinear equations described by Eq. (40) are solved using the Newton–Raphson iterative scheme, yielding the following *linearized* form of the system of equations about a configuration ${}^1\boldsymbol{U}^{(i)}_{n+1}$:

$$D\boldsymbol{R}({}^1\boldsymbol{U}^{(i)}_{n+1})\Delta^1\boldsymbol{U} = -\boldsymbol{R}({}^1\boldsymbol{U}^{(i)}_{n+1}), \tag{41}$$

where $n+1$ represents the current loading step and $i+1$ is the current Newton iteration. The tangent operator is obtained by consistent linearization of the residual Eq. (40), for the constitutive model described in Section 3.1, and is given by

$$D\boldsymbol{R}({}^1\boldsymbol{U}^{(i)}_{n+1})\Delta^1\boldsymbol{U} = \frac{1}{|\Theta|}\mathop{\mathbb{A}}_{e=1}^{N_{\mathrm{el}}}\Bigg[\underbrace{\int_{\Theta^e}\boldsymbol{B}^{\mathrm{T}}(1-\omega_{n+1})^A\boldsymbol{L}\boldsymbol{B}\,\mathrm{d}\Theta^e}_{\text{secant part}} - \underbrace{\int_{\Theta^e}\boldsymbol{B}^{\mathrm{T}\,A}\boldsymbol{L}\boldsymbol{B}^1\boldsymbol{U}^{(i)}_{n+1}\otimes\frac{\partial\omega_{n+1}}{\partial\,{}^1\boldsymbol{U}^{(i)}_{n+1}}\,\mathrm{d}\Theta^e}_{\text{tangent correction part}}$$
$$+\underbrace{\int_{\Theta^e}\boldsymbol{B}^{\mathrm{T}0}\boldsymbol{\varepsilon}\otimes\frac{\partial\omega_{n+1}}{\partial^1\boldsymbol{U}^{(i)}_{n+1}}\,\mathrm{d}\Theta^e}_{\text{macro-scale contribution}}\Bigg]\Delta^1\boldsymbol{U}, \tag{42}$$

where

$$\frac{\partial \omega_{n+1}}{\partial^1 \boldsymbol{U}_{n+1}^{(i)}} = \frac{\partial \omega_{n+1}}{\partial \bar{Y}_{n+1}} \frac{\partial \bar{Y}_{n+1}}{\partial^1 \boldsymbol{\varepsilon}_{n+1}} \frac{\partial^1 \boldsymbol{\varepsilon}_{n+1}}{\partial^1 \boldsymbol{U}_{n+1}^{(i)}}. \tag{43}$$

The linearization of the damage law (first term on the right-hand side of Eq. (43)) is delineated in Appendix A.

To control the accuracy of the time integration of the constitutive response, an adaptive time-stepping procedure is required. The technique used in the current implementation is similar to one described by Lush et al. (1989). The maximum increment in the damage parameter at any integration point, $\Delta\omega_{\max}$, is monitored to control the size of the loading step. The details of the load-stepping procedure are given in Appendix B.

4. Bounds on the multiscale cohesive response

In this section, we investigate the upper and lower bounds on the multiscale cohesive solution by analyzing a $3000 \times 300\,\mu\text{m}$ cell with 30.15 % particle volume fraction (see insert of Fig. 4(a)). The micro-structure consists of 54 particles with a 40 μm diameter. The bounds on the multiscale cohesive solution are analyzed by considering 2D plane strain conditions and two different constitutive behaviors: (1) a material that hardens and (2) a material that initially hardens and then softens. The loading rate in Y_3-direction is kept constant at ${}^0\varepsilon_{33} = 0.1\,\text{s}^{-1}$ for both cases.

4.1. Hardening material

The individual cohesive response of matrix and inclusion along with the bounds are depicted in Fig. 4(a). The matrix phase is assumed to be three times stiffer than the particles. The material properties are listed in Table 1. The traction-separation curves labeled "matrix" and "particle" are obtained by applying the

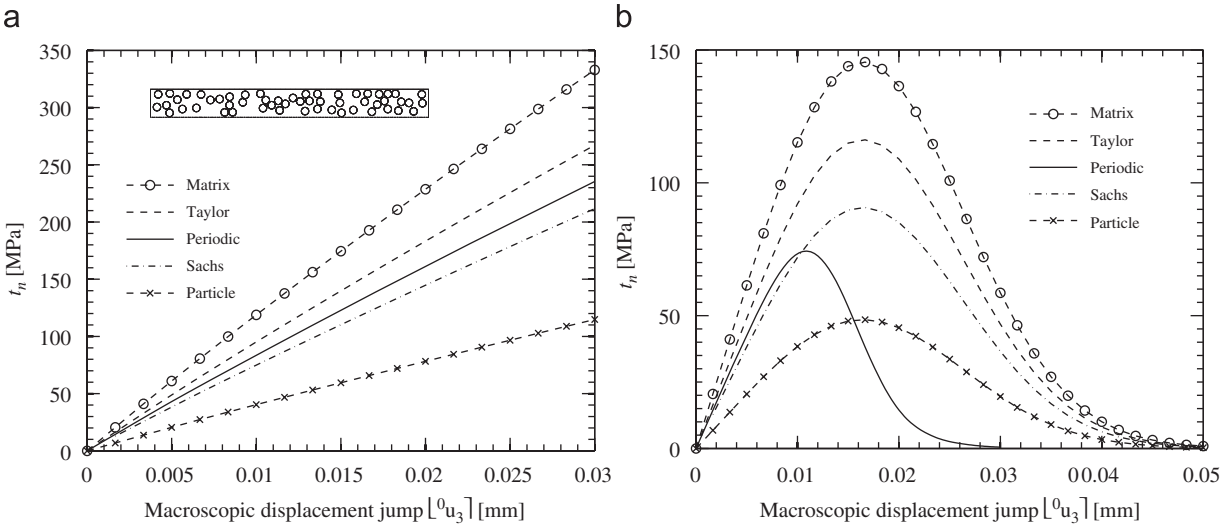

Fig. 4. Bounds on the multiscale semi-periodic cohesive solution in (a) hardening and (b) hardening-softening regimes. The inset in the figure (a) shows the geometry of the adhesive semi-periodic cell from which the bounds are extracted.

Table 1
Material properties used to compute the bounds for a hardening material

	E (GPa)	ν	Y_{in} (J/m^3)	p_1	p_2	μ (1/s)
Matrix	2.4	0.34	0.32	30000.0	0.35	19.0
Inclusion	0.8	0.34	0.32	30000.0	0.35	19.0

Table 2
Material properties used in bound analysis with a softening material

	E (GPa)	v	Y_{in} (J/m^3)	p_1	p_2	μ (1/s)
Matrix	2.4	0.34	0.3	30.0	1.3	19.0
Inclusion	0.8	0.34	0.1	30.0	1.3	19.0

multiscale cohesive scheme to homogeneous adhesive layers made of the individual phases (23). The Taylor solution (Taylor, 1938) represents the upper bound on the multiscale response, while the Sachs solution (Sachs, 1928) forms the lower bound. The Taylor bound corresponds to a constant strain condition or uniform rate of deformation, i.e., $\nabla^{\text{s}}_{Y}{}^{1}\boldsymbol{u} = \boldsymbol{0}$ within the micro-structure. Substituting this condition in Eq. (22), the Taylor bound, $\mathscr{C}^{\text{Taylor}}$, can be computed exactly. The upper bound turns out to be the *weighted* mean of individual material properties with the weights equal to the volume fractions of each constituent phase. On the other hand, the lower bound, $\mathscr{C}^{\text{Sachs}}$, denotes a constant-stress condition within the micro-structure and is given by the *harmonic* mean of individual constituent properties. The problem is driven by the constant stress condition in each phase, the strain in individual phases is then computed by invoking the constitutive relationship. The corresponding macroscopic jump can be computed by taking the volume average. We see that the effective multiscale properties ($\mathscr{C}^{\text{MC}}$) are well confined within the Taylor and Sachs bounds, i.e., $\mathscr{C}^{\text{Sachs}} < \mathscr{C}^{\text{MC}} < \mathscr{C}^{\text{Taylor}}$. The multiscale solution is solved using semi-periodic boundary conditions (periodicity only for left and right edges) and the micro-scale fluctuation displacement ${}^{1}\boldsymbol{u}(\boldsymbol{Y}) \in \mathscr{V}_{\Theta}$, as defined in Eq. (4).

4.2. Softening material

More relevant to the multiscale analysis of the cohesive failure response is the second, softening case, modeled with material properties shown in Table 2. Although, the bounds are quite well understood for hardening materials (Talbot and Willis, 1985, 1992), the bounds for softening materials are still open question, at least to authors' knowledge. Here, we do not intend to establish mathematically rigorous bounds, but rather report on the numerical solutions only. More detailed study would be required to prove that the solution is bounded, if even such a claim is relevant or can be made. As in the previous case, the matrix is assumed to be three times stiffer than the inclusions. The individual cohesive response of matrix and inclusion are depicted in Fig. 4(b). Both phases harden after crossing the linear elastic regime and then experience softening. The material properties for these phases are so chosen that the maximum stress occurs at the same value of strain. The Taylor and Sachs bounds can be computed exactly as mentioned previously. The multiscale solution is observed to obey the micro-mechanics bounds in the hardening regime, while in the softening region the multiscale solution lies below the Sachs solution. This can be attributed to loss of ellipticity of governing equation in the softening region. Physically, this implies that a heterogeneous material has less failure resistance in the softening regime than the corresponding constant stress condition.

5. Illustrative examples

We now turn our attention to a set of adhesive failure problems illustrating how the multiscale cohesive framework described in Sections 2 and 3 can relate micro-structural damage evolution to the macroscopic cohesive response of heterogeneous layers made of circular inclusions. Although, the theoretical framework presented in this work is 3D, the illustrative examples described in this section are solved in a 2D (plane strain) setting. In the model problems described hereafter, the interface between the embedded particles and the surrounding matrix is assumed to be perfect and the damage evolution in both phases is captured with the isotropic rate-dependent damage model described in Section 3.1. The loading rate is kept constant for all loading cases (mode I or mixed mode) such that ${}^{0}\dot{\varepsilon}_{33} = 0.1\,\text{s}^{-1}$, ${}^{0}\dot{\varepsilon}_{23} = 0.1\,\text{s}^{-1}$ and $\lfloor {}^{0}u_2 \rceil / \lfloor {}^{0}u_3 \rceil = 1.0$ for mixed loading. The properties of the two components are chosen to simulate two failure scenarios: (1) soft particles in a stiff brittle matrix, (2) stiff brittle particles in a soft matrix. The primary focus of this illustrative study is to show how the very different failure processes taking place at the micro-scale for these two failure scenarios

affect the overall cohesive response of the adhesive as predicted by the multiscale formulation. Although, the micro-scale domain selected in all the simulations is large enough to capture the relevant physics, we make no claim regarding the representativeness of the domain (with respect to the RVE size). One would need to compute the bounds on the solution with respect to the cell size to determine the representativeness of results.

5.1. Soft particles in a stiffer, brittle matrix

The constitutive response of the matrix and inclusion phases is shown in Fig. 5. The material properties, listed in Table 3, have been chosen to model soft, ductile particles embedded in a (three times) stiffer but brittle matrix. Two random particle distributions are considered, as illustrated in Fig. 6 and in Table 4, which also provides information on the finite element discretization adopted for the two heterogeneous adhesive layers. The particle volume fraction V_f is kept almost constant (at about 22.4%), but the particle size (and therefore their number) is varied.

For all problems studied in this paper, the finite element discretization is chosen to provide a spatially converged solution. The temporal convergence is guarded by a fully implicit nonlinear solver and the adaptive time stepping procedure discussed in Section 3.2 and Appendix B. The desired incremental value of the damage parameter $\Delta\omega_d$ is set to 0.125. The spatial and temporal convergence of the finite element solution is demonstrated in Fig. 7 for the 40-particle case subjected to mode I loading. This particular case is further investigated in Fig. 8(a), which presents the macroscopic traction-separation law for the mode I case and the evolution of damage taking place at the micro-scale for the three states A, B, and C marked on the macroscopic response. In all three micro-scale contour plots, the displayed quantity, the damage parameter ω, ranges from 0 to 1; 0 being the undamaged state and 1 representing the fully damaged condition. State A corresponds to the failure strength of the composite. Although damage is still limited in the heterogeneous layer, stress concentrations are observed especially in regions of higher particle concentrations due to the proximity between inclusions. The nucleated micro-cracks progressively coalesce, leading to a network of

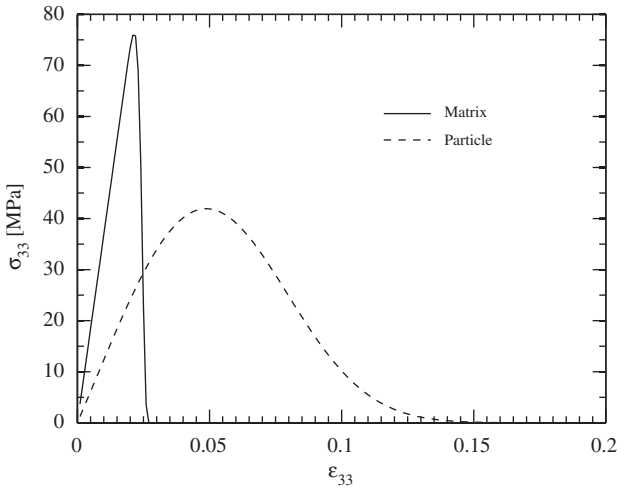

Fig. 5. Constitutive response of adhesive matrix and particle inclusions. The material properties used are listed in Table 3. Above material behavior corresponds to an uniaxial strain condition with a strain rate of $\dot{\varepsilon} = 0.1\,\mathrm{s}^{-1}$.

Table 3
Material properties for soft particle/stiff matrix example

	E (GPa)	ν	Y_{in} (J/m^3)	p_1	p_2	μ (1/s)
Matrix	2.4	0.34	0.32	2.5	8.0	19.0
Inclusion	0.8	0.34	0.1	30.0	1.3	19.0

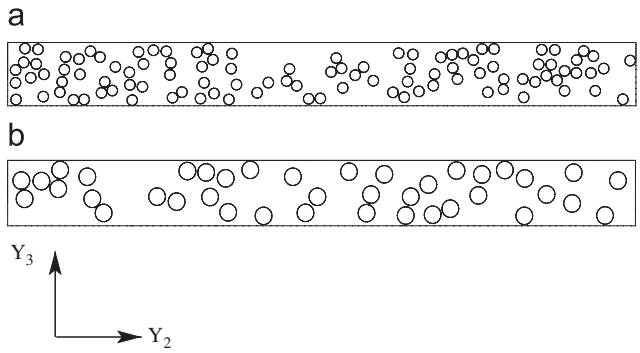

Fig. 6. Semi-periodic unit cells for heterogeneous adhesives composed of (a) 103 50 μm diameter particles ($V_f = 22.42\%$) and (b) 40 80 μm diameter particles ($V_f = 22.34\%$).

Table 4
Geometrical and finite element discretization details for the two heterogeneous layers shown in Fig. 6

	# of particles	Diameter (μm)	V_f (%)	# elements	# nodes
Fig. 6(a)	103	50.0	22.42	45 490	23 112
Fig. 6(b)	40	80.0	22.34	27 926	14 310

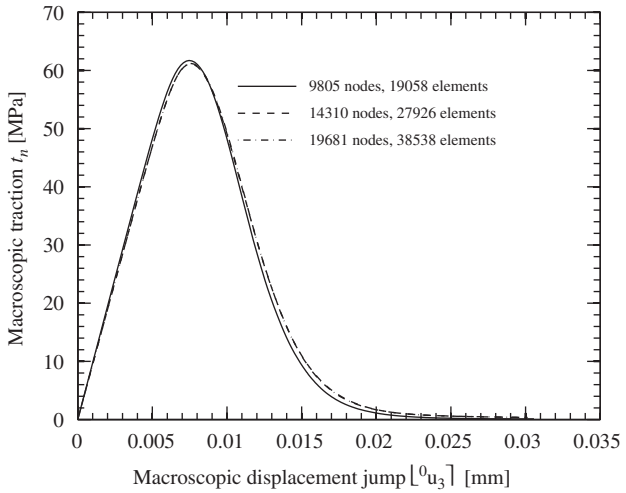

Fig. 7. Spatial convergence study for the 40-particle case.

larger cracks that form discrete damage zones and weaken the adhesive layer (Point B), thereby reducing its cohesive strength. While the initial failure took place in the stiffer, more brittle matrix, damage quickly appears in the particles as well. Upon further loading, the damage zones act as dominant cracks, leading to the complete failure of the adhesive layer (Point C). Note the complexity of the failure process at the micro-scale, which includes branching as apparent in the upper left corner of the cell. The crack path is dictated by the distribution of the particles. One of the micro-cracks becomes dominant and the associated strain localization unloads other parts of the adhesive unit cell. Throughout the failure process, the damage distribution is periodic as prescribed by the boundary conditions along the left and right edges of the adhesive unit cell.

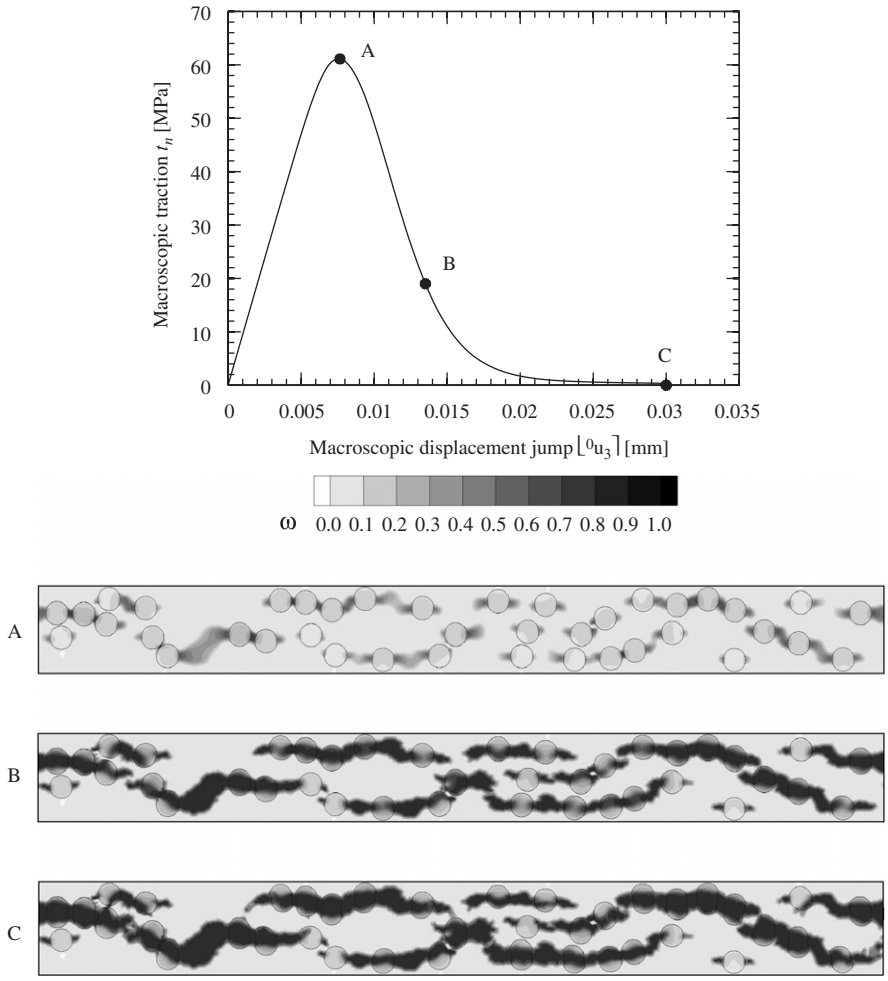

Fig. 8. Macroscopic traction-separation law (top) for the 40-particle case. The damage patterns corresponding to points A, B and C on the macroscopic cohesive law are also shown.

The multiscale cohesive framework can also be used to extract, in a natural way, the mixed-mode failure response of heterogeneous adhesives, as illustrated in Fig. 9, which shows the evolution of the macroscopic normal, t_{n}, and tangential, $t_{\mathrm{t}} = \sqrt{t_{t1}^2 + t_{t2}^2}$, cohesive tractions versus the normal, $\lfloor {}^0u_3 \rceil$, and tangential, $\lfloor {}^0u_t \rceil = \sqrt{\lfloor {}^0u_1 \rceil^2 + \lfloor {}^0u_2 \rceil^2}$, displacement jumps. Recall that due to the plane strain assumption, $\lfloor {}^0u_1 \rceil = 0$, and due to orientation of the normal, $t_{t1} = 0$. For the chosen level of mode mixity (kept constant throughout the loading process), the computed failure strength in shear is substantially smaller than its normal counterpart. It is likely that this result is an outcome of the simple isotropic damage model used to capture the progressive failure of the matrix and the particles. A more sophisticated anisotropic damage model would need to be adopted at the micro-scale to capture the increased resistance to shear failure. The damage pattern associated with the complete mixed-mode failure of micro-structure is shown in Fig. 10. Although it also involves the coalescence of micro-cracks through the particles and the matrix, the failure pattern is quite different from that obtained in the mode I case, primarily in terms of the orientation of the micro-cracks. Note the localization apparent from the deformed periodic boundaries of the adhesive layer.

By repeating the failure process under a range of mode mixity, the cohesive failure envelope can be extracted as displayed in Fig. 11, clearly illustrating the combined effect of the normal and tangential failure modes on the fracture properties of the adhesive layer. Due to the variational character of our multiscale model, even for

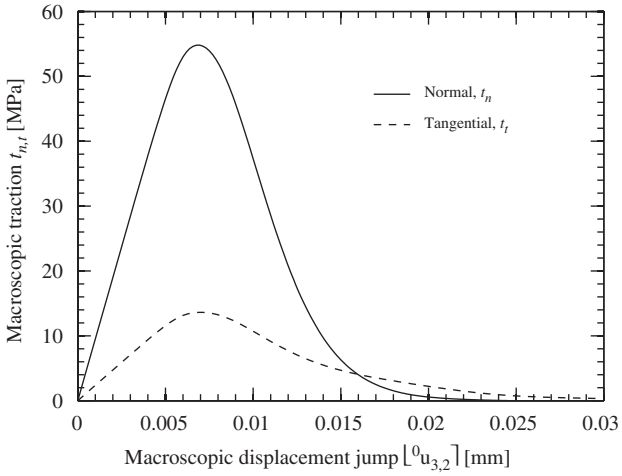

Fig. 9. Normal and tangential macroscopic traction response for 40-particle mixed mode case ($\lfloor {}^0u_2 \rceil / \lfloor {}^0u_3 \rceil = 1.0$). Here we plot the normal and tangential tractions as a function of normal and tangential opening displacement, respectively.

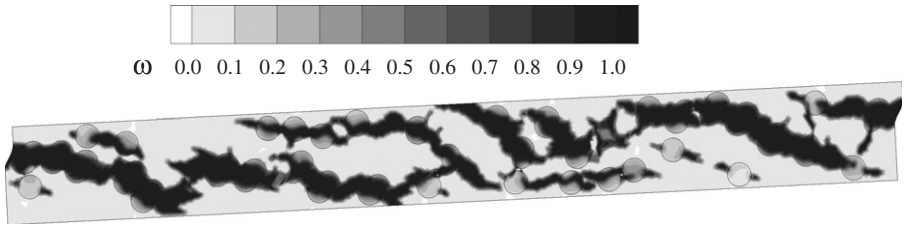

Fig. 10. Damage pattern for 40-particle cell under mixed mode loading.

the random distribution of the circular inclusions, an outcome of the multiscale cohesive scheme is the anti-symmetric shear failure response, often assumed in phenomenological cohesive laws. It should be noted that the cohesive failure envelope, shown in Fig. 11, has been computed by following failure paths with fixed level of mode mixity, i.e., by following a set of rays (centered at the origin) in the $(\lfloor {}^0u_2 \rceil, \lfloor {}^0u_3 \rceil)$ space. Due to the nonlinearity of the damage process, a different path in the above space is likely to yield a different damage map, and thus the envelop can only be used as an approximate model at the macroscale. The fully coupled micro- and macro-analysis, which is a part of our future research, would be required to obtain the exact macroscopic response.

5.1.1. *Effect of particle size*

To study the effect of particle size on the macroscopic properties, we compare the failure responses of the 40- and 130-particle cells described in Fig. 6 and Table 4. As shown in Fig. 12, the macroscopic failure responses for these two adhesive systems are almost identical, both under mode I and mixed-mode conditions. The failure patterns are, however, somewhat distinct, as illustrated in Figs. 13(a) for the 130-particle case (to be compared with their 40-particle counterparts, Figs. 8 and 10). As the number of particles increases, the number of nucleation sites increases, leading to a larger number of micro-cracks, many of which get arrested as a few critical ones coalesce. However, these differences at the micro-scale do not appear to affect the macroscopic failure response of the adhesive. This similarity between the solid and dashed curves in Fig. 12 likely stems from the absence of a direct length scale in the isotropic damage model adopted in this study and from the highly distributed nature of the damage processes taking place in the heterogeneous adhesive. By incorporating a cohesive law along the particle–matrix interface, a natural failure length scale that captures the effect of particle size can be introduced, as demonstrated by Tan et al. (2005). It is worth pointing out,

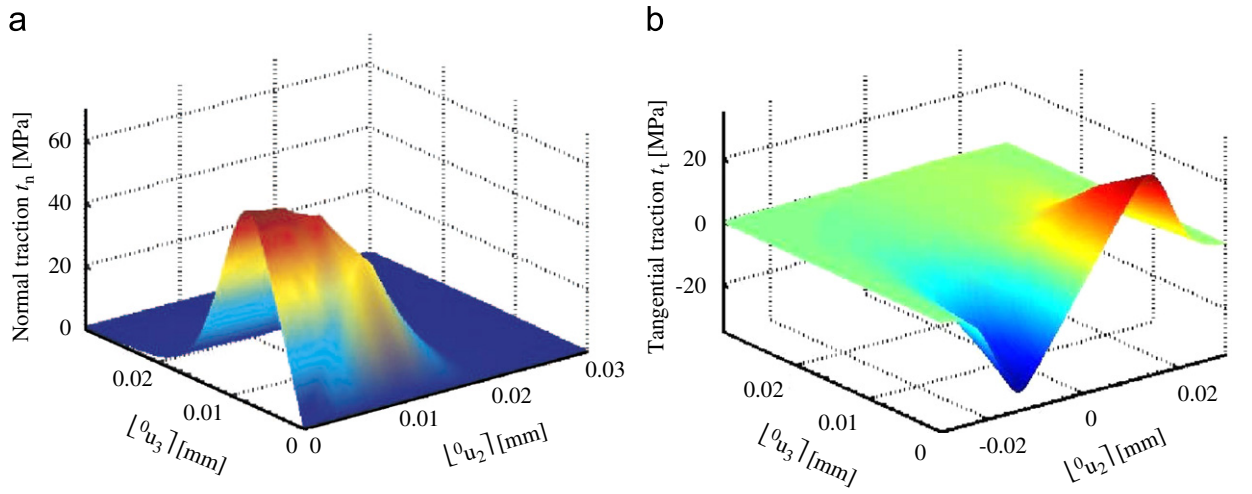

Fig. 11. Cohesive damage envelope for (a) normal and (b) tangential macroscopic traction components.

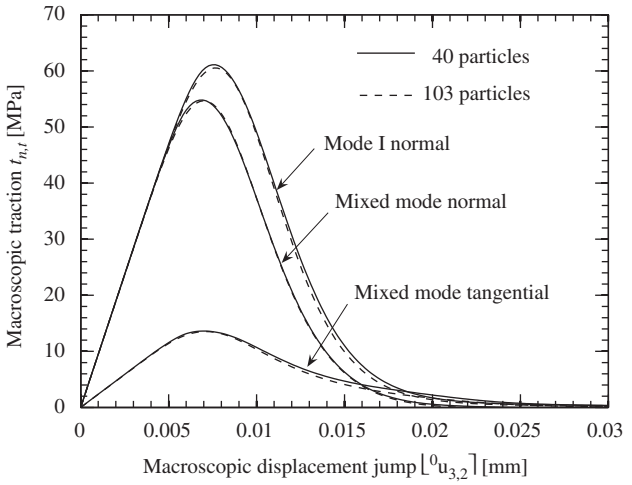

Fig. 12. Comparison of macroscopic traction-separation law for 103-particle and 40-particle cells with equal volume fraction.

however, that, regardless of the particle size, the nature of the damage taking place in a heterogeneous layer with soft particles appears to be entirely cohesive (adhesive fails rather than bond between the adhesive layer and an adherend, which we refer to as adhesive failure).

5.1.2. *Effect of volume fraction*

Focusing on the effect of volume fraction on the macroscopic cohesive properties, we now investigate 11 random micro-structures with particle volume fraction ranging from 2.79% to 30.15%. We assume that every periodic unit cell has a random particle distribution, with the statistical effect of the particle distributions quantified by considering for every volume fraction five cells with different particle arrangements. The macroscopic traction-separation curves for a few representative cases (5 of 11) are shown in Fig. 14. Those are computed as mean of five runs for each cell with error bars corresponding to the standard deviation. Since the inclusions are softer than the surrounding matrix, the elastic modulus decreases with increasing volume fraction. The tensile failure strength $t_{\max}$ follows a similar trend, dropping from close to 80 MPa for

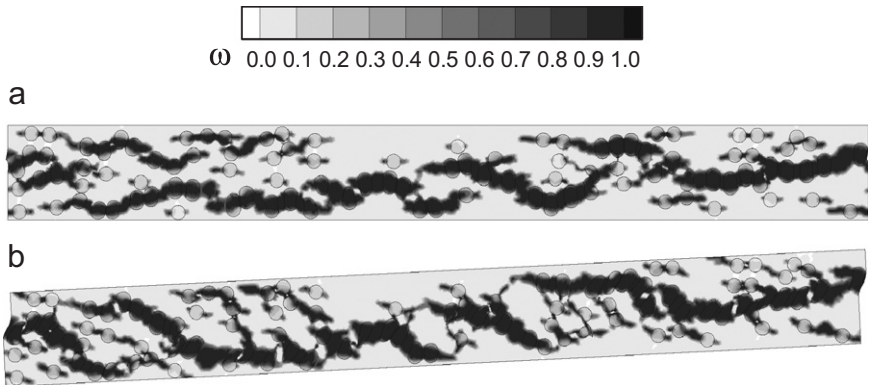

Fig. 13. Damage pattern for fully failed 103-particle cell under (a) mode I and (b) mixed-mode loading.

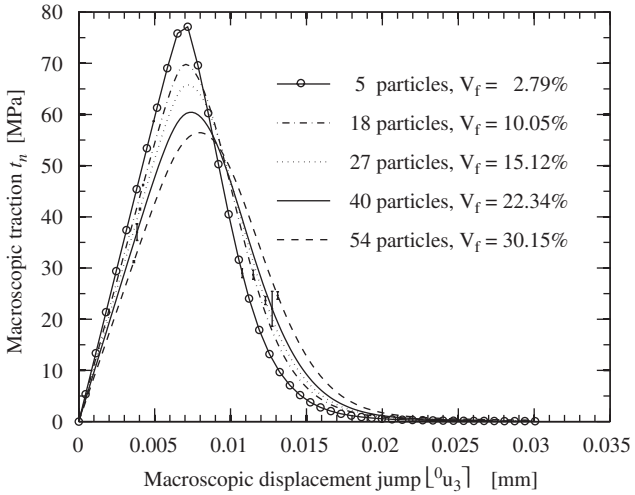

Fig. 14. Effect of volume fraction on the mode I traction-separation response of a heterogeneous adhesive with soft particles embedded in a brittle matrix.

$V_f = 2.79\%$ to less than 60 MPa for $V_f = 30.15\%$. The value of macroscopic displacement jump, at which the peak cohesive traction occurs, shifts to the right with increasing particle volume fraction. These effects can be directly related to the individual constitutive response of the matrix and the particles (see Fig. 5).

The amount of energy spent in the fracture process at the micro-scale can be computed by integrating the area under the traction-separation law as

$$G_{Ic} = \int_0^{\lfloor {}^0u \rceil_f} t_n(\lfloor {}^0\boldsymbol{u} \rceil)\, \mathrm{d}\lfloor {}^0u_3 \rceil, \tag{44}$$

where G_{Ic} denotes the mode I fracture toughness and $\lfloor {}^0u \rceil_f$ is the displacement jump associated with the complete failure of the adhesive layer. The effect of the volume fraction on the mode I fracture toughness is shown in Fig. 15(a). Displayed curve represents mean, and the error bars have been obtained again by computing the standard deviation of fracture toughness for five different particle distributions for each case. To understand this result, let us start by noticing that the failure energy of the particles exceeds that of the matrix (Fig. 5). With an increase in the volume fraction of particles, the fracture toughness of the adhesive is then expected to increase, at least initially, as apparent in Fig. 15(a). However, with further increase in volume fraction, the particles act as stress concentrators and favor micro-cracks propagation resulting in a reduced

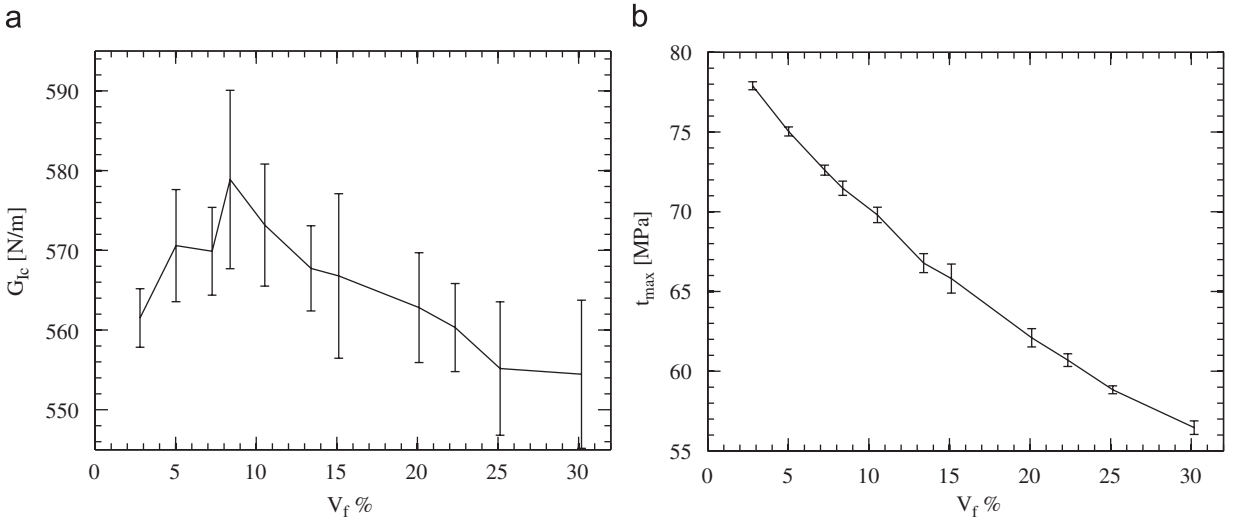

Fig. 15. Effect of volume fraction on the mode I (a) fracture toughness and (b) fracture strength. The error bars correspond to the standard deviation associated with the five randomly generated cells of each volume fraction.

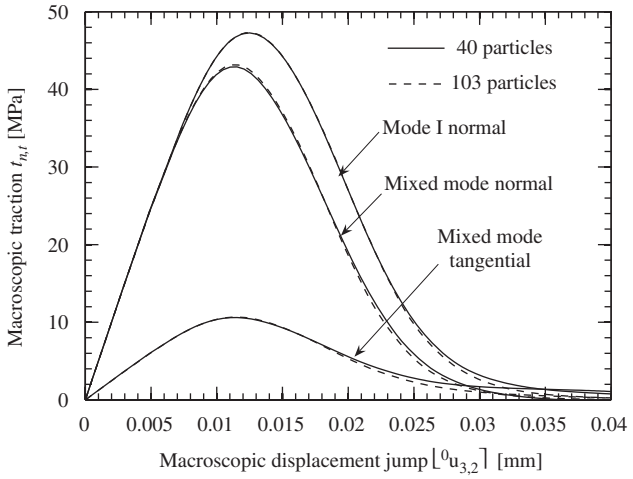

Fig. 16. Macroscopic traction-separation law for stiff 40-particle case.

fracture toughness. It should be noted that the large size of the error bars is associated with the limited range of G_{Ic} values displayed on the vertical axis.

Fig. 15(b) shows the effect of volume fraction on the maximum tensile cohesive strength, $t_{\max}$, of the heterogeneous adhesive (mean and standard deviation is shown). As expected, the maximum strength decreases with the volume fraction, as was alluded to in Fig. 14.

5.2. *Hard brittle particles in a soft matrix*

The material properties for the model problem involving stiff particles embedded in a softer matrix are chosen by simply switching the matrix and inclusion properties adopted for the soft-particle example described in the previous subsection, allowing for a more direct comparison with the soft-particle case results. The geometry and discretization of the unit cell for the adhesive are the same as those used for the soft-particle case (see Fig. 6 and Table 4).

As was the case for the soft-particle problem, the mode I and mixed-mode macroscopic cohesive failure response of the heterogeneous adhesives with stiff particles (Fig. 16) shows almost no dependence on the particle size. However, a direct comparison between the soft-particle case results (Fig. 12), and those obtained with the stiff inclusions (Fig. 16), yields some important differences between these two cases. The predicted failure strength is significantly lower than in the previous case, while the value of the displacement jump vector at which the cohesive tractions reach their peak is substantially higher for stiff particles than for soft inclusions. These differences can be traced to the damage obtained at the micro-scale shown in Figs. 17 and 18 for the 40- and 103-particle cases, respectively. The key difference is associated with the fact that, in the stiff-particle case, the failure takes place almost exclusively in the matrix. The particles still play the role of stress concentrators that initiate matrix cracking. However, while damage ran through the soft particles, the micro-cracks tend to propagate around the stiffer and stronger particles, which act as obstacles. This leads to a much more distributed damage in the unit cell compared to the soft-particle system.

Another important observation relative to the micro-scale damage process is the fact that failure in the stiff-particle case takes place in a more adhesive fashion (i.e., that damage tends to be more concentrated along the top and bottom edges of the adhesive layer) than in its soft-inclusion counterpart. This is particularly true in the mixed-mode situation and in regions where the particle clustering makes adhesive failure more energetically favorable. Note that, in this study, the adherent/adhesive interface has been assumed to be very strong, and adhesive failure can only be achieved through the propagation of micro-cracks through the matrix material in the immediate vicinity of the top and bottom edges of the adhesive layer. A more detailed study of this competition between adhesive and cohesive failure might require a different failure

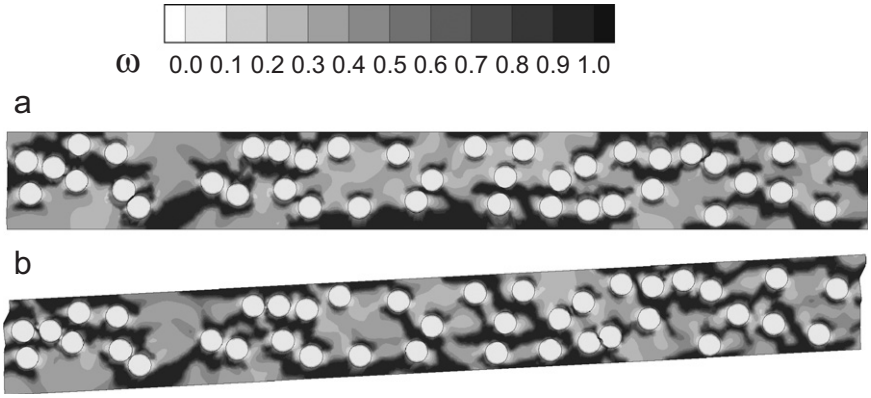

Fig. 17. Damage pattern for 40-particle case with stiff particles under (a) mode I and (b) mixed mode loading.

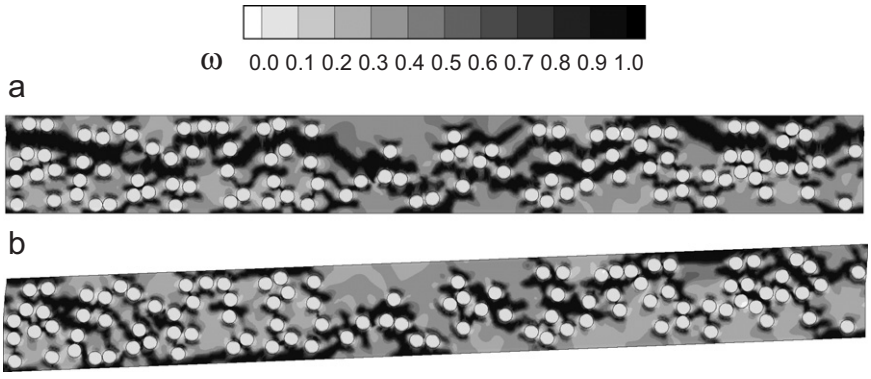

Fig. 18. Damage pattern for 103-particle case with stiff particles in soft matrix under (a) mode I and (b) mixed mode loading.

model for the adherent/adhesive interface, but the role of particle clustering, alluded to in this model problem, is likely to persist.

6. Conclusions

A multiscale cohesive model capable of linking the micro-scale failure events in heterogeneous thin layers to the macroscopic constitutive relationship has been developed and implemented. The model relies on the Hill's energy equivalence lemma for bridging the micro- and macro-scales within the computational homogenization scheme. A simple isotropic damage constitutive relation has been used to model the failure of heterogeneous adhesives. The classical micro-mechanics bounds on the multiscale cohesive solution in the hardening as well as the softening region have been presented. The robustness of the framework has been demonstrated by solving several examples, including various model heterogeneous adhesive layers with stiff and soft particles subjected to a range of loading conditions. Through these examples, we have demonstrated how the multiscale cohesive framework can be used to extract physically based macroscopic constitutive law from micro-scale failure processes. The multiscale cohesive framework is not specific to the damage model considered in this study and can readily be applied to a wide range of damage models used to capture the failure processes taking place at the micro-scale.

Acknowledgments

This work is supported by the National Science Foundation under Grant Number CMS 0527965. The authors also gratefully acknowledge support from the Center for Simulation of Advanced Rockets (CSAR) at the University of Illinois, Urbana-Champaign. Research at CSAR is funded by the U.S. Department of Energy as a part of its Advanced Simulation and Computing (ASC) program under contract number B523819.

Appendix A. Integration algorithm and consistent linearization for viscous damage model

To integrate the evolution equations (39) we employ the implicit backward Euler integration scheme. Thus the equations of evolution are solved incrementally over a sequence of given time steps $[\mathrm{t}_n, \mathrm{t}_{n+1}] \subset \mathbb{R}^+, n = 0, 1, 2, \ldots$ with initial conditions $\{\boldsymbol{\tau}, \omega, \chi\}|_{\mathrm{t}=\mathrm{t}_n} = \{\boldsymbol{\tau}_n, \omega_n, \chi_n\}$. The time step is given by $\Delta\mathrm{t} = \mathrm{t}_{n+1} - \mathrm{t}_n$.

Algorithm 1. Rate-dependent damage integration algorithm.

1 Compute $\bar{Y}_{n+1} = \frac{1}{2}{}^{A}\boldsymbol{\varepsilon}_{n+1} : {}^{A}\boldsymbol{L} : {}^{A}\boldsymbol{\varepsilon}_{n+1}$

2 Check $g = G(\bar{Y}_{n+1}) - \chi_n > 0$?

NO $\rightarrow$ no damage within this time step *EXIT*

YES $\rightarrow$ rate-dependent damage loading *CONTINUE*

3 Compute ω_{n+1} and χ_{n+1}

$$\omega_{n+1} = \omega_n + \frac{\Delta\mathrm{t}\,\mu}{1 + \Delta\mathrm{t}\mu}[G(\bar{Y}_{n+1}) - \chi_n]$$

$$\chi_{n+1} = \frac{\chi_n + \Delta\mathrm{t}\,\mu G(\bar{Y}_{n+1})}{1 + \Delta\mathrm{t}\mu}$$

4 Update stress

$$\bar{\boldsymbol{\tau}}_{n+1} = {}^{A}\boldsymbol{L} : {}^{A}\boldsymbol{\varepsilon}_{n+1}$$

$$\boldsymbol{\tau}_{n+1} = (1 - \omega_{n+1})\bar{\boldsymbol{\tau}}_{n+1}$$

Note that since $0 \leqslant \mu \leqslant \infty$ the state variable χ^{t} is properly bounded, $\chi_n \leqslant \chi_{n+1} \leqslant G(\bar{Y}_{n+1})$, between the instantaneous elastic and inviscid damage limits.

The numerical scheme as describe in Section 3.2 is implicit and thus consistent linearization is important if one wants to maintain a quadratic rate of convergence, when Newton's type algorithm

is employed to solve the system of nonlinear equations. The linearized term associated with the damage law is given by

$$\frac{\partial \omega_{n+1}}{\partial \bar{Y}_{n+1}} = \frac{\Delta t \mu}{1 + \Delta t \mu} \frac{\partial G}{\partial \bar{Y}_{n+1}}, \tag{A.1}$$

where

$$\frac{\partial G}{\partial \bar{Y}} = \frac{p_2}{p_1 Y_{\text{in}}} \exp\left[-\left(\frac{\bar{Y} - Y_{\text{in}}}{p_1 Y_{\text{in}}} \right)^{p_2} \right] \left(\frac{\bar{Y} - Y_{\text{in}}}{p_1 Y_{\text{in}}} \right)^{p_2 - 1}. \tag{A.2}$$

Appendix B. Adaptive load-stepping scheme

The automatic time-stepping algorithm (Lush et al., 1989) can be operated to keep the ratio

$$\alpha = \frac{\Delta \omega_{\max}}{\Delta \omega_{\text{d}}} \tag{B.1}$$

approximately equal to 1.0 by adjusting the size of time step. In above, $\Delta\omega_{\text{d}}$ is desired increment in damage parameter, a user input. The following algorithm is used to adjust the size of time step:

Algorithm 2. Adaptive load-stepping.

1 If $0.8 < \alpha \leqslant 1.25$ then $\Delta t_{n+1} = \Delta t_n \alpha$
2 If $0.5 < \alpha \leqslant 0.8$ then $\Delta t_{n+1} = 1.25 \Delta t_n$
3 If $\alpha \leqslant 0.5$ then $\Delta t_{n+1} = 1.5 \Delta t_n$

References

Bensoussan, A., Lions, J., Papanicolaou, G., 1978. Asymptotic Analysis for Periodic Structures. North-Holland, New York.

Bittnar, Z., Šejnoha, J., 1996. Numerical Methods in Structural Engineering. ASCE Press, New York.

Bouchitte, G., Lidouh, A., Suquet, P., 1991. Boundary homogenization and modeling of friction between a non linear deformable body and a rigid body. C. R. Acad. Sci. Paris Ser. 1 Math. 313 (13), 967–972.

Camacho, G., Ortiz, M., 1996. Computational modelling of impact damage in brittle materials. Int. J. Solid Struct. 33, 2899–2938.

Chew, H., Guo, T., Cheng, L., 2004. Vapor pressure and residual stress effects on the toughness of polymeric adhesive joints. Eng. Fract. Mech. 71, 2435–2448.

de Moura, M., Daniaud, R., Magalhães, A., 2006. Simulation of mechanical behavior of composite bonded joints containing strip defects. Int. J. Adhes. Adhes. 26, 464–473.

Dean, G., Crocker, L., Read, B., Wright, L., 2004. Prediction of deformation and failure of rubber-toughened adhesive joints. Int. J. Adhes. Adhes. 24, 295–306.

Ferracin, T., Landis, C., Delannay, F., Pardoen, T., 2003. On the determination of cohesive zone properties of an adhesive layer from the analysis of wedge-peel test. Int. J. Solids Struct. 80, 2889–2904.

Ferreira, J., Silva, H., Costa, J., Richardson, M., 2005. Stress analysis of lap joints involving natural fiber reinforced interface layers. Composites B 36, 787–795.

Geubelle, P.H., Baylor, J., 1998. Impact-induced delamination of composites: a 2d simulation. Composites B 29B, 589–602.

Hill, R., 1985. On the micro-to-macro transition in constitutive analyses of elastoplastic response at finite strain. Math. Proc. Cambridge Philos. Soc. 98, 579–590.

Hughes, T., 1995. Multiscale phenomena: Green's functions, the Dirichlet-to-Neumann formulation, subgrid scale models, bubbles and the origins of stabilized methods. Comput. Methods Appl. Mech. Eng. 127, 387–401.

Ju, J., 1989. On energy-based coupled elastoplastic damage theories: constitutive modeling and computational aspects. Int. J. Solids Struct. 25 (7), 803–833.

Lebon, F., Ould Khaoua, A., Licht, C., 1998. Numerical study of soft adhesively bonded joints in finite elasticity. Comput. Mech. 21, 134–140.

Lebon, F., Rizzoni, R., Ronel-Idrissi, S., 2004. Asymptotic analysis of some non-linear soft thin layers. Comput. Struct. 82, 1929–1938.

Lemaitre, J., 1985. Coupled elasto-plastic and damage constitutive equations. Comput. Methods Appl. Mech. Eng. 51, 31–49.

Licht, C., Michaille, G., 1997. A modelling of elastic adhesive bonded joints. Adv. Math. Sci. Appl. 7 (2), 711–740.

Lubarda, V., Krajcinovic, D., 1995. Some fundamentals issues in rate theory of damage-elastoplasticity. Int. J. Plasticity 11, 763–797.

Lubliner, J., 1972. On thermodynamic foundations of non-linear solid mechanics. Int. J. Non-Linear Mech. 7, 237–254.

Lubliner, J., 1973. On the structure of the rate equations of materials with internal variables. Acta Mech. 17, 109–119.
Lush, A., Weber, G., Anand, L., 1989. An implicit time-integration procedure for a set of internal variable constitutive equations for isotropic elasto-viscoplasticity. Int. J. Plasticity 5, 521–549.
Matouš, K., 2003. Damage evolution in particulate composite materials. Int. J. Solids Struct. 40, 1489–1503.
Matouš, K., Dvorak, G., 2002a. Design of prestressed skin/flange assembly. J. Sandwich Struct. Mater. 4 (4), 367–387.
Matouš, K., Dvorak, G., 2002b. Stress redistribution in skin/flange assemblies. Mech. Adv. Mater. Struct. 9 (3), 293–308.
Meguid, S., Sun, Y., 2004. On the tensile and shear strength of nano-reinforced composite interfaces. Mater. Design 25, 289–296.
Miehe, C., Schröder, J., Becker, M., 2002. Computational homogenization analysis in finite elasticity: material and structural instabilities on the micro- and macro-scales of periodic composites and their interaction. Comput. Methods Appl. Mech. Eng. 191, 4971–5005.
Needleman, A., 1990b. An analysis of decohesion along an imperfect interface. Int. J. Fract. 42, 21–40.
Pijaudier-Cabot, G., Bažant, Z., 1987. Non-local damage theory. J. Eng. Mech. 113, 1512–1533.
Sachs, G., 1928. Zur ableitung einer filessbedingung. Z. Ver. Dtsch. Ing., 734–736.
Shi, X.Q., Zhang, X.R., Pang, J.H.L., 2006. Determination of interface fracture toughness of adhesive joint subjected to mixed-mode loading using finite element method. Int. J. Adhes. Adhes. 26, 249–260.
Simo, J., Ju, J., 1987a. Strain- and stress-based continuum damage models—i. formulation. Int. J. Solids Struct. 23 (7), 821–840.
Simo, J., Ju, J., 1987b. Strain- and stress-based continuum damage models—ii. computational aspects. Int. J. Solids Struct. 23 (7), 841–869.
Talbot, D., Willis, J., 1985. Variational principles for inhomogeneous nonlinear media. IMA J. Appl. Math. 35, 39–54.
Talbot, D., Willis, J., 1992. Some simple explicit bounds for the overall behavior of nonlinear composites. Int. J. Solids Struct. 29, 1981–1987.
Tan, H., Huang, Y., Liu, C., Geubelle, P., 2005. The Mori–Tanaka method for composite materials with nonlinear interface debonding. Int. J. Plasticity 21, 1890–1918.
Taylor, G., 1938. Plastic strain in metals. J. Inst. Met. 62, 307–324.
Wells, G., Sluys, L., 2001. A new method for modelling cohesive cracks using finite elements. Int. J. Numer. Methods Eng. 50, 2667–2682.
White, S., Sottos, N., Geubelle, P., Moore, J., Kessler, M., Sriram, S., Brown, E., Viswanathan, S., 2001. Autonomic healing of polymer composites. Nature 409, 794–797.
Xu, S., Dillard, D., Dillard, J., 2003. Environmental aging effects on the durability of electrically conductive adhesive joints. Int. J. Adhes. Adhes. 23, 235–250.
Zhao, Q., Hoa, S.V., 2007. Toughening mechanism of epoxy resins with micro/nano particles. J. Compos. Mater. 41, 201–219.
Zhao, W., Ramani, K., Mueller, B., 2000. Processing and fracture behavior of a polyethylene-based thermoplastic adhesive and a glass-fiber filled epoxy adhesive. Int. J. Adhes. Adhes. 20, 409–413.